

# First-principles and experimental analysis of $f^n-f^{n-1}d^1$ absorption spectra and multiplet energy levels of $\text{Pr}^{3+}$ , $\text{Nd}^{3+}$ , and $\text{U}^{3+}$ in $\text{LiYF}_4$

Shinta Watanabe,<sup>1,2,\*</sup> Kazuyoshi Ogasawara,<sup>2</sup> Masahito Yoshino,<sup>3</sup> and Takanori Nagasaki<sup>4</sup>

<sup>1</sup>Venture Business Laboratory, Nagoya University, Furo-cho, Chikusa-ku, Nagoya, Aichi 464-8603, Japan

<sup>2</sup>Department of Chemistry, School of Science and Technology, Kwansei Gakuin University, 2-1 Gakuen, Sanda, Hyogo 669-1337, Japan

<sup>3</sup>Department of Materials, Physics and Energy Engineering, Graduated School of Engineering, Nagoya University, Furo-cho, Chikusa-ku, Nagoya, Aichi 464-8603, Japan

<sup>4</sup>EcoTopia Science Institute, Nagoya University, Furo-cho, Chikusa-ku, Nagoya, Aichi 464-8603, Japan

(Received 28 May 2009; revised manuscript received 12 January 2010; published 29 March 2010)

We performed experimental and theoretical investigation of the  $f^n-f^{n-1}d^1$  transitions of  $\text{Pr}^{3+}$ ,  $\text{Nd}^{3+}$ , and  $\text{U}^{3+}$  in  $\text{LiYF}_4$ . The  $4f^2-4f^15d^1$  absorption spectra for  $\text{Pr}^{3+}$  in  $\text{LiYF}_4$  and the  $4f^3-4f^25d^1$  absorption spectra for  $\text{Nd}^{3+}$  in  $\text{LiYF}_4$  were measured using a synchrotron radiation light source at several different temperatures while the  $5f^3-5f^26d^1$  absorption spectra for  $\text{U}^{3+}$  in  $\text{LiYF}_4$  referred to report of Hubert *et al.* The multiplet energy levels and  $f^n-f^{n-1}d^1$  absorption spectra were calculated by a first-principles four-component relativistic configuration-interaction method. For all calculations of  $\text{Nd}^{3+}$  and  $\text{U}^{3+}$  in  $\text{LiYF}_4$ , we used the Dirac-Coulomb-Breit Hamiltonian and the molecular spinors obtained from the relativistic Vosko-Wilk-Nusair potential. The overall features of the theoretical absorption spectra of both  $\text{Nd}^{3+}$  and  $\text{U}^{3+}$  in  $\text{LiYF}_4$  reproduced the experimental features well. The origins of the experimental absorption spectra were clarified by performing a configuration analysis based on the many-electron wave functions. The splitting between peaks were affected by both spin-orbit interaction of  $f$  orbitals and crystal-field splitting of  $d$  orbitals. We found that the oscillator strengths of the  $4f^3-4f^25d^1$  transition for  $\text{Nd}^{3+}$  in  $\text{LiYF}_4$  are slightly larger than those of the  $5f^3-5f^26d^1$  transition for  $\text{U}^{3+}$  in  $\text{LiYF}_4$ . The experimental absorption spectra for  $\text{Nd}^{3+}$  in  $\text{LiYF}_4$  measured at nine different temperatures indicated that the  $4f^3-4f^25d^1$  absorption spectra for  $\text{Nd}^{3+}$  in  $\text{LiYF}_4$  have no significant temperature dependence. For  $\text{Pr}^{3+}$  in  $\text{LiYF}_4$ , we performed more detailed investigations. The lattice relaxation effects due to the substitution of  $\text{Y}^{3+}$  by  $\text{Pr}^{3+}$  were estimated using a first-principles density-functional calculation. Structural optimization calculations indicated that the local structure of the  $\text{Pr}^{3+}$  site was slightly distorted. Overall, the theoretical  $4f^2-4f^15d^1$  absorption spectra reproduced the experimental spectra. The experimental absorption spectra were investigated by configuration analysis based on the many-electron wave functions. The theoretical calculations indicated that the temperature dependence of the experimental spectra was due to both thermal excitation and phonon effects. In addition, we also investigated the effects of the exchange-correlation interaction and the Breit term by comparing the results from six different Hamiltonians.

DOI: [10.1103/PhysRevB.81.125128](https://doi.org/10.1103/PhysRevB.81.125128)

PACS number(s): 71.55.-i, 71.15.Rf, 42.70.Hj, 71.10.-w

## I. INTRODUCTION

Trivalent praseodymium ( $\text{Pr}^{3+}$ )- and neodymium ( $\text{Nd}^{3+}$ )-doped  $\text{LiYF}_4$  has been widely studied for application as a luminescent material in devices such as solid-state visible-light lasers.<sup>1-6</sup> The  $4f^n-4f^{n-1}$  ( $n=2$  for  $\text{Pr}^{3+}$  and  $n=3$  for  $\text{Nd}^{3+}$ ) intraconfiguration transitions of  $\text{Pr}^{3+}$  and  $\text{Nd}^{3+}$  were mainly utilized for these materials. Because of strong recent desire for luminescent materials in high-energy regions, the  $4f^n-4f^{n-1}5d^1$  interconfigurational transitions of  $\text{Pr}^{3+}$  and  $\text{Nd}^{3+}$  in wide band-gap host crystals have drawn attention for potential application as luminescent materials in devices such as tunable solid-state lasers or UV and VUV phosphors. Since  $\text{LiYF}_4$  is a promising host for solid-state laser crystals,  $\text{Pr}^{3+}$ - and  $\text{Nd}^{3+}$ -doped  $\text{LiYF}_4$  has been extensively investigated, both experimentally and theoretically.<sup>7-24</sup>

In the case of trivalent uranium ( $\text{U}^{3+}$ ), although  $\text{U}^{3+}$ -doped  $\text{CaF}_2$  and  $\text{SrF}_2$  have been studied for use in solid-state lasers in the infrared (IR) region,<sup>25,26</sup> studies for the  $5f^3-5f^3$  and  $5f^3-5f^26d^1$  transitions remain limited. This is because uranium is a radioactive element and the trivalent state is not its most stable valence.<sup>27</sup>  $\text{U}^{3+}$ -doped  $\text{LiYF}_4$  has also been investigated as a good candidate for IR lasers.<sup>28-34</sup>

In much of the previous theoretical research of lanthanides (Ln) and actinides (An) in host crystals or glasses, crystal-field theory (CFT) has been widely used to analyze energy levels and optical properties.<sup>9-13,22,34-37</sup> Although this approach is quite useful, and can reproduce the experimental spectra and estimate some meaningful physical parameters, it cannot be used for nonempirical prediction of the local structure around doped ions or of optical properties, since it requires several empirical parameters and experimental spectra to be fit.

For nonempirical analysis of these properties, a first-principles approach is necessary. The first-principles analysis of the electronic structure of impurities in crystals based on density-functional theory (DFT) has recently been improved considerably. This method is quite useful for the estimation of structural or optical properties on the basis of structural features.<sup>38-47</sup> In addition, it is a powerful tool for the analysis of  $K$ -edge x-ray absorption near-edge structure (XANES) or electron-energy-loss near-edge structure (ELNES) spectra.<sup>48-50</sup>

However, first-principles analysis of the multiplet structures and optical properties of Ln impurities in crystals based on the explicit many-electron wave functions remains lim-

ited, and has been performed by only a few groups.<sup>51–57</sup> Our group has investigated the optical properties of Ln impurities in host crystals using a first-principles method.<sup>58–66</sup> In these calculations, the lattice relaxation around doped-Ln ions due to the substitution of cations by Ln ions were either neglected or were considered only by a simple correction of bond lengths using Shannon's ionic radii.<sup>67</sup> However, in the case of  $\text{Ce}^{3+}$ -doped  $\text{LiYF}_4$ , we reported that consideration of the explicit local structure around  $\text{Ce}^{3+}$  was crucial to an accurate understanding of the optical properties, which depend on the local structure of the impurity ions.<sup>66</sup>

In this work, we present the fundamental applications of the many-electron calculation for the multiplet energy levels and absorption spectra of  $\text{Nd}^{3+}$  and  $\text{U}^{3+}$  in  $\text{LiYF}_4$ . Four-component relativistic first-principles configuration-interaction (CI) calculations<sup>68</sup> were performed. This calculation method has been successfully applied to the investigation of  $4f^n-4f^{n-1}5d^1$  transitions<sup>65</sup> of rare-earth ions and  $L_{2,3}$ -edge XANES and ELNES spectra of transition-metal ions.<sup>68–72</sup>

In more detailed investigations, we examined  $\text{Pr}^{3+}$  in  $\text{LiYF}_4$ , including the lattice relaxation process in theoretical study. The Shannon's ionic radius of  $\text{Pr}^{3+}$  is about 110.5% that of  $\text{Y}^{3+}$ .<sup>67</sup> Therefore, it is important to estimate the lattice relaxation due to the substitution of  $\text{Y}^{3+}$  by  $\text{Pr}^{3+}$  in  $\text{Pr}^{3+}$ -doped  $\text{LiYF}_4$  crystal. In this work, pseudopotential plane wave calculations were performed to estimate the effects of lattice relaxation. The local structure around  $\text{Pr}^{3+}$  in  $\text{LiYF}_4$  was optimized using first-principles total-energy minimization by the CASTEP code.<sup>73–75</sup> The scalar relativistic effects were taken into account, that is, the relativistic effects for core electrons were included in the pseudopotentials. In addition, in the present calculations, we used a relaxed cluster model constructed from the optimized structure. For comparison, we also used a cluster model with a simple isotropic relaxation estimated from the Shannon's ionic radii and an unrelaxed model. The origin of the peaks in the absorption spectrum was investigated by comparing the theoretical absorption spectra with the experimental ones and by configuration analysis of the many-electron wave functions. The effects of lattice relaxation on the  $4f-5d$  absorption spectra were also examined by comparing the theoretical spectra of different structural models.

Experimentally, we measured the  $4f^n-4f^{n-1}5d^1$  absorption spectra for  $\text{Pr}^{3+}$  and  $\text{Nd}^{3+}$  in  $\text{LiYF}_4$  using a synchrotron radiation (SR) light source at several temperatures. The excitation spectrum for  $\text{Pr}^{3+}$  and  $\text{Nd}^{3+}$  in  $\text{LiYF}_4$  was measured previously.<sup>9,11</sup> However, since the spectral shapes of an excitation spectrum depend on the monitored emission wavelength, the measured spectrum could not be compared directly with the theoretical absorption spectrum. To enable comparison with theoretical spectra, the measurement of the absorption spectra is quite important. In this paper, we present the comprehensive investigation of the  $f^n-f^{n-1}d^1$  transitions of  $\text{Pr}^{3+}$ ,  $\text{Nd}^{3+}$ , and  $\text{U}^{3+}$  in  $\text{LiYF}_4$ , using both first-principles calculations and experiments with a SR light source.

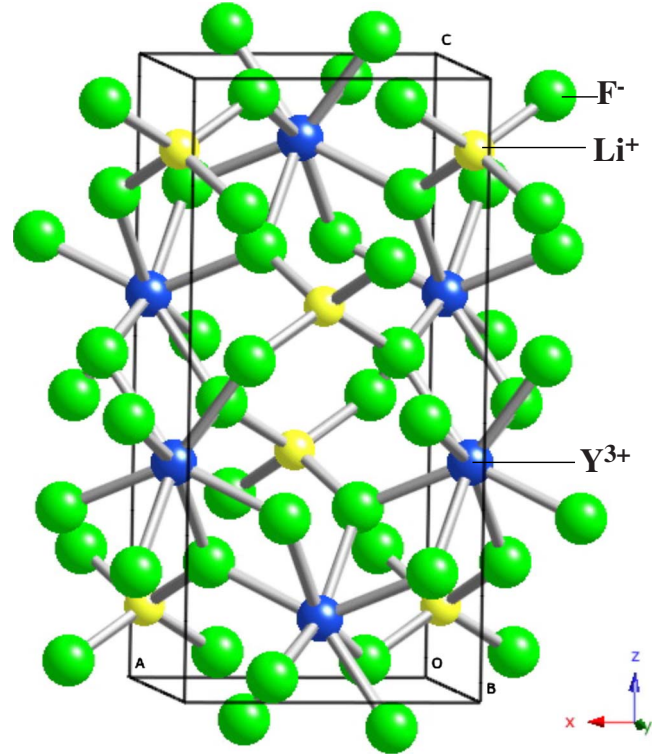


FIG. 1. (Color online) The crystal structure of pure  $\text{LiYF}_4$  crystal.

## II. COMPUTATIONAL PROCEDURE

### A. Crystal structure of $\text{LiYF}_4$

Figure 1 shows the crystal structure of  $\text{LiYF}_4$ , which is known as the inverse scheelite structure,<sup>76</sup> in which  $\text{Y}^{3+}$  is coordinated by eight  $\text{F}^-$  ions and  $\text{Li}^+$  is coordinated by four  $\text{F}^-$  ions. The space group is  $I4_1/a$ , the crystal system is tetragonal, and the lattice constants are  $a=5.164$  Å and  $c=10.741$  Å. The unit cell contains 24 atoms. Considering the ionic radius, valency, and charge compensation,  $\text{Pr}^{3+}$  is expected to substitute for the  $\text{Y}^{3+}$  site. The point group of the  $\text{Y}^{3+}$  site is  $S_4$ , and the Y-F bond lengths are 2.244 Å for four of the bonds and 2.297 Å for the other four.

### B. Estimation of lattice relaxation

The effects of lattice relaxation due to the substitution of  $\text{Y}^{3+}$  by  $\text{Pr}^{3+}$  were estimated by a first-principles total-energy calculation using the CASTEP code,<sup>73–75</sup> which is based on the ultrasoft pseudopotential plane-wave method. We adopted the Vanderbilt form ultrasoft pseudopotentials<sup>77</sup> throughout the present work. The orbitals explicitly treated as the valence state were  $1s$  and  $2s$  for Li;  $4d$ ,  $5s$ , and  $5p$  for Y;  $2s$  and  $2p$  for F; and  $4f$ ,  $5s$ ,  $5p$ , and  $6s$  for Pr. The exchange-correlation potential was considered within the generalized gradient approximation proposed by Perdew, Burke, and Ernzerhof.<sup>78</sup> The cutoff energy of the plane wave was 500 eV, and the Brillouin zone was sampled on the  $6 \times 6 \times 3$  Monkhorst-Pack grid for pure  $\text{LiYF}_4$  unit-cell calculations and the  $3 \times 3 \times 3$  Monkhorst-Pack grid for  $\text{Pr}^{3+}$ -doped  $\text{LiYF}_4$  supercell calculations.<sup>79</sup> The numerical error was estimated

to be less than 1 meV/atom by cutoff and  $k$ -point convergence tests. To evaluate the accuracy of the structural optimization, the lattice parameters and all atomic positions in the unit cell of a pure LiYF<sub>4</sub> crystal were estimated by this approach and compared to experimental values. Next, we optimized the local structure around Pr<sup>3+</sup> ions in Pr<sup>3+</sup>-doped LiYF<sub>4</sub>. In this calculation, one Pr<sup>3+</sup> ion in the  $2 \times 2 \times 1$  supercell, which contains 96 atoms and corresponds to 6.25% of the Y<sup>3+</sup> ions in LiYF<sub>4</sub>, was substituted by a Pr<sup>3+</sup> ion. All atomic positions were relaxed with the lattice parameters fixed at the theoretical values for pure LiYF<sub>4</sub> obtained above. In this model, we assumed that there were no significant interactions between Pr<sup>3+</sup> ions, such as the cooperative Jahn-Teller effect, because the closest Pr<sup>3+</sup>-Pr<sup>3+</sup> distance was 10.3843 Å, indicating that Pr<sup>3+</sup> ions were relatively separated. Geometry optimization was performed until the residual forces and stresses dropped below 0.01 eV/Å and 0.02 GPa, respectively.

### C. Multiplet energy levels and absorption spectrum

The  $4f^n-4f^{n-1}5d^1$  transitions of Pr<sup>3+</sup>, Nd<sup>3+</sup>, and U<sup>3+</sup> in LiYF<sub>4</sub> were investigated using the relativistic CI method.<sup>68</sup> In this first-principles CI calculation, the multiplet energy levels and absorption spectrum were calculated using  $MF_8^{5-}$  ( $M=\text{Pr, Nd, and U}$ ) model clusters. An effective Madelung potential was also considered by locating several thousand point charges at atomic sites outside the cluster. An undesirable electronic dipole generated by the point charges was removed by the Evjen method.<sup>80</sup> Lattice relaxation effects due to the substitution of Y<sup>3+</sup> by Pr<sup>3+</sup> were also considered using the optimized structure estimated by the above method. The relativistic CI method used in the present work was similar to that used in Ref. 68, except for several improvements to the exchange-correlation potential and the Coulomb interaction.

First, four-component relativistic molecular orbital (MO) spinors were obtained using a relativistic DFT calculation, in which the four-component Dirac equation was solved directly. These four-component relativistic MO spinors were expressed as linear combinations of atomic-orbital (AO) spinors.<sup>81</sup> In the present calculation, instead of the Dirac-Fock-Slater approximation used in Ref. 68, the exchange-correlation potential  $V_{\text{XC}}(\mathbf{r})$  within the local-density approximation (LDA) proposed by Vosko, Wilk, and Nusair (VWN) (Ref. 82) and its relativistic formalism proposed by MacDonald and Vosko (RVWN) (Ref. 83) were considered. In this paper, these exchange-correlation potentials are referred to as VWN and RVWN potentials, respectively.

After these one-electron relativistic DFT calculations, many-electron calculations were performed using the obtained relativistic MO spinors. Since the CI calculations for all  $N$  electrons in a cluster required a prodigious quantity of computational time and resources, only MOs mainly composed of Ln  $4f$  and  $5d$  or An  $5f$  and  $6d$  orbitals were explicitly considered in the many-electron calculation. The many-electron Dirac-Coulomb (DC) Hamiltonian  $H_{\text{DC}}$  can be expressed as

$$H_{\text{DC}} = \sum_i^n h_{\text{D}}(\mathbf{r}_i) + \sum_i^n \sum_{j>i}^n V_{ee}(\mathbf{r}_i, \mathbf{r}_j), \quad (1)$$

where  $n$  is the number of electrons in the active space of the CI calculation and  $\mathbf{r}_i$  is the position of the  $i$ th electron. The first and second terms of  $H_{\text{DC}}$  represent the one-electron and two-electron operators, respectively. The one-electron Dirac operator  $h_{\text{D}}$  can be expressed as

$$h_{\text{D}}(\mathbf{r}_i) = c\tilde{\alpha}\mathbf{p}_i + \tilde{\beta}c^2 - \sum_{\nu} \frac{Z_{\nu}}{|\mathbf{r}_i - \mathbf{R}_{\nu}|} + V_0(\mathbf{r}_i) + \sum_{\mu} \frac{Z_{\mu}^{\text{eff}}}{|\mathbf{r}_i - \mathbf{R}_{\mu}|}, \quad (2)$$

where  $c$  is the velocity of light,  $\mathbf{p}_i$  is the momentum operator,  $\tilde{\alpha}$  and  $\tilde{\beta}$  are the Dirac matrices,  $Z_{\nu}$  and  $\mathbf{R}_{\nu}$  are the charge and position of the  $\nu$ th nucleus, and  $Z_{\mu}^{\text{eff}}$  and  $\mathbf{R}_{\mu}$  are the effective charge and position of the  $\mu$ th ion outside the model cluster.  $V_0(\mathbf{r}_i)$  in Eq. (2) denotes the Coulomb and exchange-correlation potential on these explicitly treated electrons from the other (core and valence) electrons. This potential  $V_0(\mathbf{r}_i)$  was derived by Watanabe and Kamimura using the Dirac-Fock-Slater approximation,<sup>84</sup> which is expressed as

$$V_0(\mathbf{r}) = \int \frac{\rho_0(\mathbf{r}')}{|\mathbf{r} - \mathbf{r}'|} d\mathbf{r}' + \frac{3}{4} \left[ \frac{\rho(\mathbf{r})V_{\text{XC}}\{\rho(\mathbf{r})\} - \rho_0(\mathbf{r})V_{\text{XC}}\{\rho_0(\mathbf{r})\}}{\rho_{\text{imp}}(\mathbf{r})} - V_{\text{XC}}\{\rho_{\text{imp}}(\mathbf{r})\} \right], \quad (3)$$

where  $\rho_{\text{imp}}$  is the charge density of the selected  $n$  electrons,  $\rho_0$  is the charge density of the other  $N-n$  electrons,  $\rho$  is the charge density of all  $N$  electrons ( $\rho = \rho_0 + \rho_{\text{imp}}$ ), and  $V_{\text{XC}}$  is the exchange-correlation potential. In the present work, we rewrote the potential  $V_0(\mathbf{r}_i)$  as the general LDA approximation, which is expressed as

$$V_0(\mathbf{r}) = \int \frac{\rho_0(\mathbf{r}')}{|\mathbf{r} - \mathbf{r}'|} d\mathbf{r}' + \left[ \frac{\rho(\mathbf{r})\varepsilon_{\text{XC}}\{\rho(\mathbf{r})\} - \rho_0(\mathbf{r})\varepsilon_{\text{XC}}\{\rho_0(\mathbf{r})\}}{\rho_{\text{imp}}(\mathbf{r})} - \varepsilon_{\text{XC}}\{\rho_{\text{imp}}(\mathbf{r})\} \right], \quad (4)$$

where  $\varepsilon_{\text{XC}}$  is the VWN or RVWN exchange-correlation energy in the present work. The two-electron operator represents electron-electron repulsion between electrons occupying the impurity states,

$$V_{ee}(\mathbf{r}_i, \mathbf{r}_j) = \frac{1}{r_{ij}}. \quad (5)$$

Electron-electron repulsions were explicitly taken into account by this two-electron operator. Although this  $H_{\text{DC}}$  does not include the relativistic effect in the two-electron operator  $V_{ee}(\mathbf{r}_i, \mathbf{r}_j)$ , it is very useful for calculation of many-electron systems. On the other hand, consideration of relativistic effects in the two-electron operator  $V_{ee}(\mathbf{r}_i, \mathbf{r}_j)$  requires the introduction of quantum electrodynamics (QED). Using QED, the derivation of the Hamiltonian for the interaction can be obtained from perturbation theory. The electron-electron repulsion term following  $1/r_{ij}$  can be expressed as, in Cou-



lomb gauge (specified by the relationship  $\nabla \cdot \mathbf{A} = 0$ , where  $\mathbf{A}$  is the vector potential),

$$B(\mathbf{r}_i, \mathbf{r}_j) = -\frac{1}{2r_{ij}} \left\{ \boldsymbol{\alpha}_i \cdot \boldsymbol{\alpha}_j + \frac{(\boldsymbol{\alpha}_i \cdot \mathbf{r}_{ij})(\boldsymbol{\alpha}_j \cdot \mathbf{r}_{ij})}{r_{ij}^2} \right\}, \quad (6)$$

where  $\boldsymbol{\alpha}_{ij}$  are Dirac matrices. The  $B(\mathbf{r}_i, \mathbf{r}_j)$  term is known as the frequency-independent Breit operator.<sup>85,86</sup> The Breit operator contains the magnetic interactions originating from orbital and spin motions, and the finite transmission speed of the signal between particles, generally regarded as the retardation effect, is also taken into account. Consequently, the Dirac-Coulomb-Breit (DCB) Hamiltonian  $H_{\text{DCB}}$  can be expressed in atomic units as

$$H_{\text{DCB}} = \sum_i^n h_{\text{D}}(\mathbf{r}_i) + \sum_i^n \sum_{j>i}^n \left[ \frac{1}{r_{ij}} - \frac{1}{2r_{ij}} \left\{ \boldsymbol{\alpha}_i \cdot \boldsymbol{\alpha}_j + \frac{(\boldsymbol{\alpha}_i \cdot \mathbf{r}_{ij})(\boldsymbol{\alpha}_j \cdot \mathbf{r}_{ij})}{r_{ij}^2} \right\} \right]. \quad (7)$$

As a result,  $H_{\text{DCB}}$  is accurate to the order of  $\alpha^2$ , whereas  $H_{\text{DC}}$  is accurate only to the order of  $\alpha^0$ .

In the present work, we examined six different types of Hamiltonian, which differed in exchange-correlation potential and in whether or not the Breit operator term was considered. Hereafter, these Hamiltonians are represented by  $H_{\text{DC-X}\alpha}$ ,  $H_{\text{DCB-X}\alpha}$ ,  $H_{\text{DC-VWN}}$ ,  $H_{\text{DCB-VWN}}$ ,  $H_{\text{DC-RVWN}}$ , and  $H_{\text{DCB-RVWN}}$ . The subscripts denote the type of many-electron Hamiltonian and the exchange-correlation potential. The subscripts DC and DCB represent Dirac-Coulomb and Dirac-Coulomb-Breit many-electron Hamiltonians, respectively. The subscripts X $\alpha$ , VWN, and RVWN represent X $\alpha$  potential, VWN exchange-correlation potential, and VWN exchange-correlation potential with relativistic effects, respectively, in the one-electron DFT-MO calculations. In addition, Eq. (3) was adopted as a Dirac-Fock-Slater approximation of the  $V_0(\mathbf{r})$  term in the one-electron operator of the many-electron Hamiltonian, and Eq. (4) was adopted as a VWN and RVWN approximation of the  $V_0(\mathbf{r})$  term.

By diagonalizing the many-electron Hamiltonians shown in Eqs. (1) and (7), we could obtain the many-electron eigenvalues and corresponding eigenvectors. Many-electron wave functions are generally expressed as a linear combination of Slater determinants,

$$\Psi_i = \sum_{p=1}^M C_{ip} \Phi_p, \quad (8)$$

where  $\Psi_i$  are the  $i$ th many-electron wave functions,  $\Phi_p$  is the  $p$ th Slater determinant,  $C_{ip}$  is a coefficient, and  $M$  is the number of Slater determinants. Since  $\text{Pr}^{3+}$  has an  $[\text{Xe}]4f^2$  electronic configuration, the number of possible Slater determinants for the  $4f^2$  and  $4f^15d^1$  configurations are 91 and 140, respectively. Therefore, 231 Slater determinants were used as the basis for the many-electron calculations of  $\text{Pr}^{3+}$ . Similarly, since  $\text{Nd}^{3+}$  and  $\text{U}^{3+}$  have  $[\text{Xe}]4f^3$  and  $[\text{Rn}]5f^3$  electronic configurations, the number of possible Slater determinants for the  $f^3$  and  $f^2d^1$  configurations are 364 and 910, respectively. Therefore, 1274 Slater determinants were

used as basis for the many-electron calculations of  $\text{Nd}^{3+}$  and  $\text{U}^{3+}$ .

To estimate the oscillator strength of the electric dipole transition for  $\text{Pr}^{3+}$ ,  $\text{Nd}^{3+}$ , and  $\text{U}^{3+}$  in  $\text{LiYF}_4$ , the general equation for oscillator strength, averaged over all directions, for the electric dipole transition between the initial state and the final state was used, and is given by<sup>87</sup>

$$I_{if} = \frac{2}{3}(E_f - E_i) \left| \langle \Psi_f | \sum_{k=1}^n \mathbf{r}_k \cdot \mathbf{e} | \Psi_i \rangle \right|^2, \quad (9)$$

where  $\Psi_i$  and  $\Psi_f$  are the many-electron wave functions for the initial and final states, and  $E_i$  and  $E_f$  are their energies. For easy comparison with experimental spectra, each level was broadened with a 0.20, 0.16, and 0.14 eV full width at half maximum (FWHM) Gaussian function for  $\text{Pr}^{3+}$ ,  $\text{Nd}^{3+}$ , and  $\text{U}^{3+}$ , respectively.

### III. EXPERIMENTAL PROCEDURE

$\text{Pr}^{3+}$ - and  $\text{Nd}^{3+}$ -doped  $\text{LiYF}_4$  single crystals were grown by the Bridgman-Stockbarger method from  $\text{LiF}$  (4N, MERCK),  $\text{YF}_3$  (4N, KANTO CHEMICAL), and  $\text{PrF}_3$  (3N, KOJUNDO CHEMICAL LABORATORY) or  $\text{NdF}_3$  (3N, Furuya Metal) powders. The ratio of  $\text{LiF}$  to  $\text{YF}_3$  in the reactant was 53:47 mol %, and the concentration of  $\text{Pr}^{3+}$  or  $\text{Nd}^{3+}$  ion in the reactant was 0.3 mol %. In addition to these powders, a tiny amount of  $\text{PbF}_2$  (4N, ACROS ORGANICS) powder was added to the reactant as a scavenger. The reactant was mixed in argon atmosphere and placed in a carbon crucible. To remove all oxygen, the crystal growth chamber in the furnace was evacuated to approximately  $10^{-4}$  Pa. The reactant was heated to 300 °C and held for 1 h, then heated to above the melting point [approximately 900 °C, the melting point of the  $\text{LiF-YF}_3$  binary system is approximately 819 °C (Ref. 88)] and held for 24 h. Finally, the sample was lowered 8 cm at a rate of approximately 1 mm/h through an approximate temperature difference of 200 °C from initial to final positions. The  $\text{Ln}^{3+}$ -doped  $\text{LiYF}_4$  sample was identified as single phase by x-ray diffraction measurement.

The  $4f^n-4f^{n-1}5d^1$  absorption spectra of  $\text{Pr}^{3+}$  and  $\text{Nd}^{3+}$  were measured using a SR light source at beam line 1B (BL-1B) of UVSOR at the Institute of Molecular Science, Okazaki, Japan. The light transmitted through the sample was detected using a photomultiplier tube (Hamamatsu R105). The absorption spectra in the VUV region were normalized by the emission of sodium salicylate. Measurements were performed at 10, 35, 50, 75, 100, 150, 200, 250, and 300 K. The measurements at low temperatures were performed using a cold cryostat and liquid helium.

### IV. RESULTS AND DISCUSSION

#### A. Molecular-orbital energy levels of $\text{Nd}^{3+}$ and $\text{U}^{3+}$ in $\text{LiYF}_4$

Figure 2 shows the calculated MO energy levels of (a)  $\text{Nd}^{3+}:\text{LiYF}_4$  and (b)  $\text{U}^{3+}:\text{LiYF}_4$  and the energy difference between the bottom of the  $d$  levels and the top of the  $f$  levels ( $E_{d\text{-bottom}} - E_{f\text{-top}}$ ), the splittings of the  $e$  and  $d$  levels are also plotted in the right panel. The fluorine  $2p$  bands correspond-

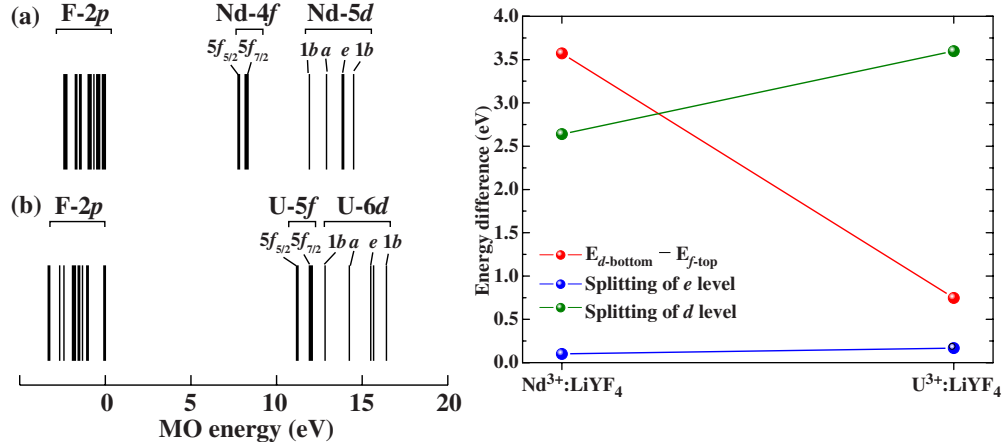


FIG. 2. (Color online) The calculated MO energy levels of (a)  $\text{Nd}^{3+}:\text{LiYF}_4$  and (b)  $\text{U}^{3+}:\text{LiYF}_4$  (left panel) and the energy difference between the bottom of the  $d$  levels and the top of the  $f$  levels ( $E_{d\text{-bottom}} - E_{f\text{-top}}$ ), splittings of the  $e$  and  $d$  levels (right panel). The RVWN potential was used for these calculations.

ing to the valence band and the top of valence bands were set at 0 eV. Each MO was labeled with the name of the most dominant AO.

The MO energy level structure of the  $f$  levels was dominated by the spin-orbit interaction, and was split into  $f_{5/2}$  and  $f_{7/2}$ , while the crystal-field splittings were very small. On the other hand, the MO energy level structure of the  $d$  levels was dominated by crystal-field splitting. The irreducible representations of the exact  $S_4$  symmetry are also shown in the figure. In the  $S_4$  symmetry, nonrelativistic MOs can be classified into irreducible representations denoted as  $a$ ,  $b$ , and  $e$ , while the four-component relativistic MO spinors can be classified into the irreducible representations of the double group denoted as  $\Gamma_{5,6}$ , and  $\Gamma_{7,8}$ . Here we used both the Mulliken notation for the nonrelativistic MOs and the Bethe symbols for the relativistic MO spinors in order to give a clear, detailed explanation. The  $d$  levels split into  $1b$ ,  $a$ ,  $e$ , and  $2b$  from the lower level in the irreducible representation of  $S_4$  symmetry. In addition, the  $e$  state split slightly due to spin-orbit interactions. As shown in Fig. 2, the splitting of the  $e$  level due to the spin-orbit interaction, and the splitting of the  $d$  levels due to crystal-field splitting was larger in  $\text{U}^{3+}:\text{LiYF}_4$  than  $\text{Nd}^{3+}:\text{LiYF}_4$ , and was 0.17, 2.64 eV for  $\text{Nd}^{3+}:\text{LiYF}_4$  and 0.10, 3.60 eV for  $\text{U}^{3+}:\text{LiYF}_4$ . In addition, the energy difference between the  $f$  and  $d$  levels for  $\text{U}^{3+}:\text{LiYF}_4$  was significantly smaller than for  $\text{Nd}^{3+}:\text{LiYF}_4$ . These values were 3.57 eV for  $\text{Nd}^{3+}:\text{LiYF}_4$  and 0.75 eV for  $\text{U}^{3+}:\text{LiYF}_4$ . As a result, the mixing between  $f$  and  $d$  states of  $\text{U}^{3+}:\text{LiYF}_4$  was larger than in  $\text{Nd}^{3+}:\text{LiYF}_4$ , while the interactions with ligand F 2p orbitals were nearly the same.

An analysis of the MO compositions was performed to investigate the chemical bonding effects of  $\text{Nd}^{3+}$  and  $\text{U}^{3+}$  in  $\text{LiYF}_4$ . These analyses were performed using Mulliken population analysis.<sup>89</sup> The compositions of each AO with dominant  $f$  or  $d$  character in  $\text{Nd}^{3+}:\text{LiYF}_4$  and  $\text{U}^{3+}:\text{LiYF}_4$  are shown in Table I. For the seven levels in the energy range 7.77–8.32 eV for  $\text{Nd}^{3+}:\text{LiYF}_4$  and 11.16–12.06 eV for  $\text{U}^{3+}:\text{LiYF}_4$ , there was little mixing between  $f_{5/2}$  and  $f_{7/2}$  states, and the results were consistent with this tendency. However, the magnitude of the mixing between  $f$  and  $d$

states was quite different between  $\text{Nd}^{3+}$  and  $\text{U}^{3+}$ . For  $\text{U}^{3+}$ , mixing between  $5f$  and  $6d$  states was relatively large at the top of the  $5f$  level. The mixing between  $f$  states and ligand F 2sp states was quite small, and denote the same tendency. The calculated results indicate that the Nd 4f states were strongly localized, and the U 5f states were relatively localized. The five levels, in the energy range 11.89–14.53 eV for  $\text{Nd}^{3+}:\text{LiYF}_4$  and 12.81–16.41 eV for  $\text{U}^{3+}:\text{LiYF}_4$ , corresponded to MOs with dominant Nd  $d$  and U  $d$  character. The mixing between the U 6d orbitals and ligand F 2sp orbitals had the same tendency as the mixing between the Nd 5d orbitals and ligand F 2sp orbitals. This indicates a stronger interaction with the ligand orbitals for the Nd  $d$  and U  $d$  orbitals than for the Nd  $f$  and U  $f$  orbitals. These results followed the same tendency as  $f^2$  configuration ions,  $\text{Pr}^{3+}$  and  $\text{U}^{4+}$ , in  $\text{LiYF}_4$ .<sup>58</sup>

## B. Multiplet energy levels and absorption spectra of $\text{Nd}^{3+}$ and $\text{U}^{3+}$ in $\text{LiYF}_4$

The calculated multiplet energy levels for (a)  $\text{Nd}^{3+}:\text{LiYF}_4$  and (b)  $\text{U}^{3+}:\text{LiYF}_4$ , corresponding to the  $f^3$  configurations, are shown in Fig. 3. The compositions of four configurations,  $(f_{5/2})^3$ ,  $(f_{5/2})^2(f_{7/2})^1$ ,  $(f_{5/2})^1(f_{7/2})^2$ , and  $(f_{7/2})^3$ , within each energy level are shown. The lengths of the lines denote the contribution of each configuration. The red, green, blue, and purple lines represent the  $(f_{5/2})^3$ ,  $(f_{5/2})^2(f_{7/2})^1$ ,  $(f_{5/2})^1(f_{7/2})^2$ , and  $(f_{7/2})^3$  configuration, respectively. In addition, Fig. 4 shows the theoretical multiplet energy levels and their configuration compositions for (a)  $\text{Nd}^{3+}:\text{LiYF}_4$  and (b)  $\text{U}^{3+}:\text{LiYF}_4$ , corresponding to the  $f^3$  (red line) and the  $f^2d^1$  configuration (blue line). (a') is an enlargement of the energy region between 10.5 and 11.0 eV for  $\text{Nd}^{3+}:\text{LiYF}_4$ . In both figures, short lines indicate a partial contribution of each configuration. For all calculations of  $\text{Nd}^{3+}$  and  $\text{U}^{3+}$  in  $\text{LiYF}_4$ , we adopted the  $H_{\text{DCB-RVWN}}$  Hamiltonian.

For the  $f^3$  configuration, the multiplet energies were overestimated by about 20%, compared to the experimental results. However, the overall multiplet structure was reproduced. All configurations were distributed over a wide

TABLE I. Compositions (%) of the MOs for (a)  $\text{Nd}^{3+}:\text{LiYF}_4$  and (b)  $\text{U}^{3+}:\text{LiYF}_4$ .

Energy (eV)	Irre. rep.	Nd $4f_{5/2}$	Nd $4f_{7/2}$	Nd $5d_{3/2}$	Nd $5d_{5/2}$	F $2sp$
7.77	$\Gamma_{5,6}$	98.6	0.4	0.0	0.0	0.8
7.80	$\Gamma_{7,8}$	98.7	0.1	0.0	0.3	0.9
7.84	$\Gamma_{5,6}$	96.0	2.6	0.0	0.3	1.1
8.21	$\Gamma_{5,6}$	0.8	98.3	0.0	0.1	0.7
8.22	$\Gamma_{7,8}$	0.0	99.0	0.0	0.0	0.8
8.23	$\Gamma_{7,8}$	0.1	98.7	0.2	0.1	0.9
8.32	$\Gamma_{5,6}$	1.9	96.0	0.5	0.1	1.4
11.89	$\Gamma_{7,8} (1b)$	0.0	0.0	45.7	51.3	3.0
12.88	$\Gamma_{5,6} (a)$	0.1	0.4	54.3	39.8	5.1
13.86	$\Gamma_{5,6} (e)$	0.1	0.1	39.2	54.1	6.4
13.96	$\Gamma_{7,8} (e)$	0.1	0.2	24.3	69.0	5.2
14.53	$\Gamma_{7,8} (2b)$	0.1	0.1	24.5	69.0	6.9

Energy (eV)	Irre. rep.	U $5f_{5/2}$	U $5f_{7/2}$	U $6d_{3/2}$	U $6d_{5/2}$	F $2sp$
11.16	$\Gamma_{5,6}$	97.6	0.9	0.0	0.1	1.0
11.19	$\Gamma_{7,8}$	96.9	0.0	0.0	1.7	1.0
11.28	$\Gamma_{5,6}$	93.1	3.2	0.0	2.3	1.2
11.92	$\Gamma_{7,8}$	0.1	95.9	2.5	0.3	0.9
11.92	$\Gamma_{5,6}$	0.7	96.5	1.0	0.6	1.0
11.96	$\Gamma_{7,8}$	0.1	96.7	1.1	0.5	1.0
12.06	$\Gamma_{5,6}$	2.0	84.3	9.1	2.9	1.4
12.81	$\Gamma_{7,8} (1b)$	0.0	1.0	49.1	46.9	3.1
14.25	$\Gamma_{5,6} (a)$	1.8	10.7	57.4	24.1	5.4
15.50	$\Gamma_{5,6} (e)$	1.5	1.4	26.6	64.2	5.9
15.67	$\Gamma_{7,8} (e)$	0.5	2.5	26.1	64.6	6.0
16.41	$\Gamma_{7,8} (2b)$	1.0	0.6	16.0	75.8	6.3

energy range, and there was strong mixing among them. Although the mixing of the four configurations of  $\text{Nd}^{3+}:\text{LiYF}_4$  had the same tendency as in  $\text{U}^{3+}:\text{LiYF}_4$ , the distributions of the multiplet energy levels were quite different. The multiplet energy levels of  $\text{U}^{3+}$  in  $\text{LiYF}_4$  were densely distributed in the energy region between about 1.5 and 6.0 eV while those of  $\text{Nd}^{3+}$  in  $\text{LiYF}_4$  were relatively discretely distributed in the energy region up to about 8 eV. In addition, the mixing ratio of each configuration differed slightly. For example, in the ground state  $^4\text{I}_{9/2}$ , the contribution of the  $(4f_{5/2})^3$  configuration of  $\text{Nd}^{3+}$  in  $\text{LiYF}_4$  was about 60.2% while the contribution of the  $(5f_{5/2})^3$  configuration of  $\text{U}^{3+}$  in  $\text{LiYF}_4$  was about 75.4%. The theoretical energy levels of the ground state  $^4\text{I}_{9/2}$  are shown in Table II, together with the results of CF calculations and experimental values.<sup>31,90</sup> Among the irreducible representations of  $S_4$  symmetry, only  $\Gamma_5$ ,  $\Gamma_6$ ,  $\Gamma_7$ , and  $\Gamma_8$  are possible for a three-electron system, while  $\Gamma_5$  and  $\Gamma_6$  or  $\Gamma_7$  and  $\Gamma_8$  are degenerate. In comparison with the experimental values, the Stark splitting was somewhat overestimated. However, the order of irreducible representations of these five levels was consistent with both the experimental values and those obtained by CFT.

As shown in Fig. 4, the mixing between the  $5f^3$  configuration and the  $5f^26d^1$  configuration of  $\text{U}^{3+}:\text{LiYF}_4$  was com-

pletely different from the mixing between the  $4f^3$  configuration and the  $4f^25d^1$  configuration of  $\text{Nd}^{3+}:\text{LiYF}_4$ . In  $\text{Nd}^{3+}:\text{LiYF}_4$ , the mixing was only observed in the energy region of 10.5–11.0 eV, which was  $^2\text{F}$  in the  $LS$  term and is shown in Fig. 3 (a'). For  $\text{U}^{3+}:\text{LiYF}_4$ , on the other hand, the mixing between these configurations was observed from low energy levels. Consequently, the configuration interaction between the  $5f^3$  configuration and the  $5f^26d^1$  configuration for  $\text{U}^{3+}:\text{LiYF}_4$  was much stronger than in  $\text{Nd}^{3+}:\text{LiYF}_4$ . In addition, another remarkable point is that the  $5f^26d^1$  configuration of  $\text{U}^{3+}:\text{LiYF}_4$  lies at a very low energy (about 2 eV). Since the  $f^3$ - $f^2d^1$  transition spectra strongly depend on the multiplet energy level structure, the  $f$ - $d$  absorption spectra would be drastically different in these materials, even though they have the same  $f^3$  electronic configuration.

Next  $f^3$ - $f^2d^1$  absorption spectra of  $\text{Nd}^{3+}$  and  $\text{U}^{3+}$  in  $\text{LiYF}_4$  from the ground state were calculated and compared with the experimental absorption spectra. Figure 5 shows the experimental and theoretical absorption spectra for (a)  $\text{Nd}^{3+}$  and (b)  $\text{U}^{3+}$  in  $\text{LiYF}_4$ . The oscillator strengths for the transitions from the lowest energy level ( $\Gamma_{7,8}$ ) of the ground state  $^4\text{I}_{9/2}$  were calculated, and the theoretical absorption spectra were obtained by convolution with a Gaussian function having 0.16 eV FWHM for  $\text{Nd}^{3+}$  in  $\text{LiYF}_4$  and 0.14 eV FWHM for

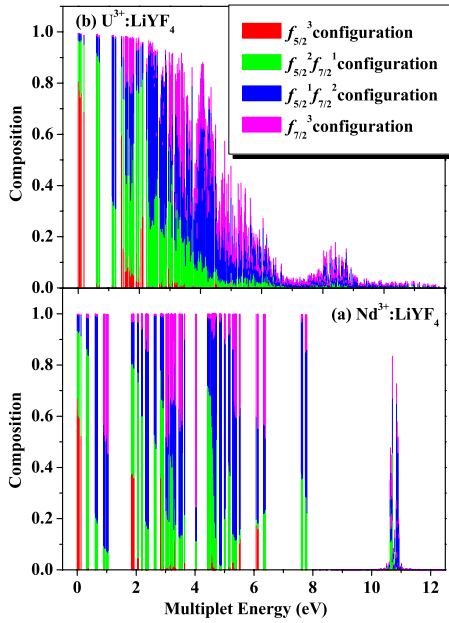


FIG. 3. (Color online) Theoretical multiplet energy levels and their configuration compositions for (a)  $\text{Nd}^{3+}:\text{LiYF}_4$  and (b)  $\text{U}^{3+}:\text{LiYF}_4$  corresponding to the  $f^3$  configuration calculated using the  $H_{\text{DCB-RVWN}}$  Hamiltonian.

$\text{U}^{3+}$  in  $\text{LiYF}_4$ . The absorption spectrum for  $\text{U}^{3+}$  in  $\text{LiYF}_4$  was measured by Simoni *et al.*<sup>32</sup> The absorption spectrum for  $\text{Nd}^{3+}$  in  $\text{LiYF}_4$  was measured at 10 K using a SR light source in the preset work.

As shown in Fig. 5, for  $\text{Nd}^{3+}$  in  $\text{LiYF}_4$ , the peaks in the theoretical absorption spectrum are denoted as A–F while peaks A–H were observed in the experimental spectrum at 10 K. Peak H can be attributed to the  $\text{LiYF}_4$  host absorption. Detailed discussion of subpeaks A' and A'' will follow. In

the case of  $\text{U}^{3+}$  in  $\text{LiYF}_4$ , the peaks in the theoretical absorption spectrum are denoted as A–J. In both spectra, the shapes and overall features were reasonably well reproduced. However, the energy separation between peaks was somewhat overestimated, although the relative peak positions were reproduced. The overestimation of the energy separation between peaks was larger in  $\text{Nd}^{3+}$  than  $\text{U}^{3+}$ . These results are related to the overestimation of the crystal fields and indicate that the lattice relaxation effects are probably larger for  $\text{Nd}^{3+}$  in  $\text{LiYF}_4$  than for  $\text{U}^{3+}$  in  $\text{LiYF}_4$ . In addition, the results indicate that the oscillator strengths of the  $4f^3-4f^25d^1$  transition for  $\text{Nd}^{3+}$  in  $\text{LiYF}_4$  are slightly larger than those of the  $5f^3-5f^26d^1$  transition for  $\text{U}^{3+}$  in  $\text{LiYF}_4$ . It seems that the increased mixing between the  $5f^3$  configurations and the  $5f^26d^1$  configurations of the  $\text{U}^{3+}$  resulted in the lower oscillator strength. These trends differed from those of the  $f^2$  configuration ions,  $\text{Pr}^{3+}$  and  $\text{U}^{4+}$ , in  $\text{LiYF}_4$ .<sup>58</sup>

The temperature dependence of the  $4f^3-4f^25d^1$  absorption spectrum for  $\text{Nd}^{3+}$  in  $\text{LiYF}_4$  was also measured using the SR light source at UVSOR. The measurements were performed at 10, 35, 50, 75, 100, 150, 200, 250, and 300 K. These absorption spectra are shown in Fig. 6. As shown in the figure, there was no clear temperature dependence. Not only the peak position energies but also the intensity ratios of peaks were nearly the same. This differed from the case of  $\text{Pr}^{3+}$  in  $\text{LiYF}_4$ , which exhibited a strong temperature dependence. For simplicity, the experimental absorption spectrum measured at 10 K was analyzed because the calculations were performed at 0 K.

In order to clarify the peak origins, configuration analysis of the many-electron wave functions was performed. The multiplet energy levels of  $\text{Nd}^{3+}$  in  $\text{LiYF}_4$  in the range 7.5–11.5 eV are shown in Fig. 7, together with the oscillator strengths and the theoretical spectrum for the transitions from the lowest level. As shown in Fig. 5, the peaks of the theoretical absorption spectrum are denoted as A–F.

Peaks A and A' mainly originate from transitions to the  $(4f_{5/2})^2(5d_{1b})^1$  configuration. The  $(4f_{5/2})^2(5d_{1b})^1$  configuration is confined within the range of 8.0–8.5 eV, and has limited interaction with the other configurations, especially the  $(4f_{5/2})^1(4f_{7/2})^1(5d_{1b})^1$  configuration. Peak A'' originates primarily from the transition to the  $(4f_{5/2})^1(4f_{7/2})^1(5d_{1b})^1$  configuration. This configuration spreads over a wide energy range and influences much higher levels. Since the transitions to the  $(4f_{5/2})^1(4f_{7/2})^1(5d_{1b})^1$  configuration, the origins of peak A', are mixed by about 30%, it is reasonable that the intensity of peak A' is weak. In addition, since the origin of peak A'' can be mainly attributed to two-electron excitations, in transitions to the  $(4f_{5/2})^1(4f_{7/2})^1(5d_{1b})^1$  configuration, the intensity should be weaker than peaks from one-electron excitations such as transitions to the  $(4f_{5/2})^2(5d_{1b})^1$  configuration. Consequently, subpeaks A' and A'' in the experimental spectrum can be attributed as indicated in Fig. 4. In other words, from the configuration analysis of the theoretical spectrum, peak A' is a shoulder of peak A, and peak A'' is a subpeak of peak A. Thus, these results indicate that the splitting between peaks A and A', A and A'' originated from spin-orbit interactions and transitions to the two-electron excitation state, based on a shake-up process. Peaks B, B', and B'' originated primarily from transitions to the

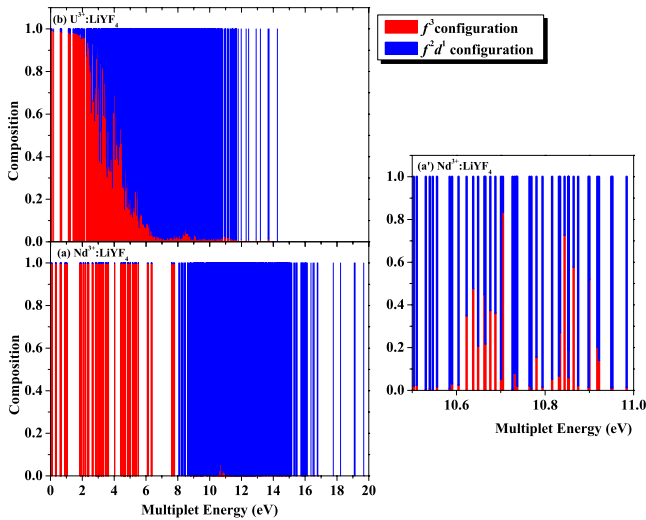


FIG. 4. (Color online) Theoretical multiplet energy levels and their configuration compositions for (a)  $\text{Nd}^{3+}:\text{LiYF}_4$  and (b)  $\text{U}^{3+}:\text{LiYF}_4$  corresponding to the  $f^3$  (red line) and the  $f^2d^1$  (blue line) configurations calculated using the  $H_{\text{DCB-RVWN}}$  Hamiltonian. (a') is an enlarged illustration in the energy region between 10.5 and 11.0 eV for  $\text{Nd}:\text{LiYF}_4$ .



TABLE II. Energy levels of the ground state  $^4I_{9/2}$  for (a)  $\text{Nd}^{3+}:\text{LiYF}_4$  and (b)  $\text{U}^{3+}:\text{LiYF}_4$ .

	Expt. <sup>a</sup>		Calc. (CFT) <sup>a</sup>		Calc. (Present work)	
	Irre. rep.	Energy (eV)	Irre. rep.	Energy (eV)	Irre. rep.	Energy (eV)
$\text{Nd}^{3+}:\text{LiYF}_4$	$^4I_{9/2}$	$\Gamma_{7,8}$	$\Gamma_{7,8}$	$\Gamma_{7,8}$	$\Gamma_{7,8}$	$\Gamma_{7,8}$
		0.0000		0.0014		0.0000
		$\Gamma_{7,8}$		0.0192		0.0356
		0.0164		0.0242		0.0367
		$\Gamma_{5,6}$		0.0312		0.0659
$\text{U}^{3+}:\text{LiYF}_4$	$^4I_{9/2}$	$\Gamma_{7,8}$	$\Gamma_{7,8}$	$\Gamma_{7,8}$	$\Gamma_{7,8}$	$\Gamma_{7,8}$
		0.0000		0.0008		0.0000
		$\Gamma_{7,8}$		0.0365		0.0434
		0.0319		0.0427		0.0581
		$\Gamma_{5,6}$		0.0635		0.0957
$\text{Nd}^{3+}:\text{LiYF}_4$		0.0226		0.0689		0.124
		$\Gamma_{5,6}$				
		0.0309				
		$\Gamma_{5,6}$				
		0.0648				
$\text{U}^{3+}:\text{LiYF}_4$		0.0511				
		$\Gamma_{5,6}$				
		0.0666				
		$\Gamma_{5,6}$				
		0.138				
		$\Gamma_{7,8}$				

<sup>a</sup>Reference 90.<sup>b</sup>Reference 31.

$(4f_{5/2})^2(5d_{1b})^1$ ,  $(4f_{5/2})^1(4f_{7/2})^1(5d_{1b})^1$ ,  $(4f_{7/2})^2(5d_{1b})^1$ ,  $(4f_{5/2})^2(5d_a)^1$ , and  $(4f_{5/2})^1(4f_{7/2})^1(5d_a)^1$  configurations. In addition, the other configurations were also slightly mixed. Therefore, the splitting between A and B peaks originated not only from crystal-field interactions but also spin-orbit

interactions. For peaks with energies higher than C, it is difficult to determine the main component of the configuration since significant configuration interaction occurs. These peaks originate from transitions to almost every configuration.

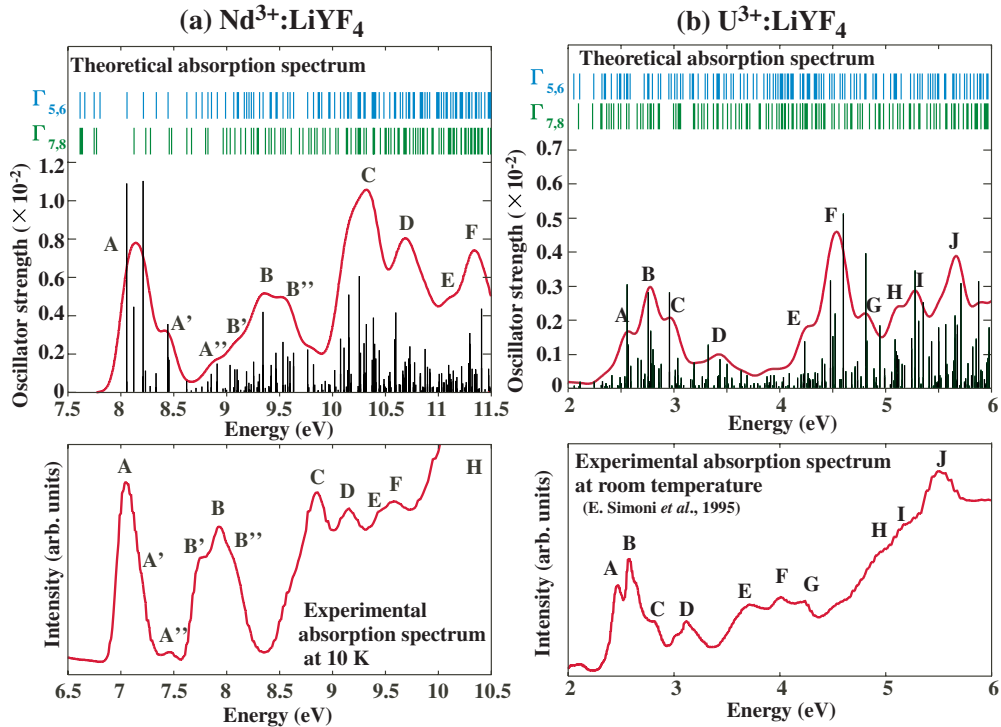


FIG. 5. (Color online) Experimental and theoretical absorption spectra for (a)  $\text{Nd}^{3+}$  in  $\text{LiYF}_4$  and (b)  $\text{U}^{3+}$  in  $\text{LiYF}_4$ . The bottom and upper panels represent the experimental and theoretical absorption spectra, respectively, along with their oscillator strengths. The theoretical spectrum was calculated using the  $H_{\text{DCB-RVWN}}$  Hamiltonian.



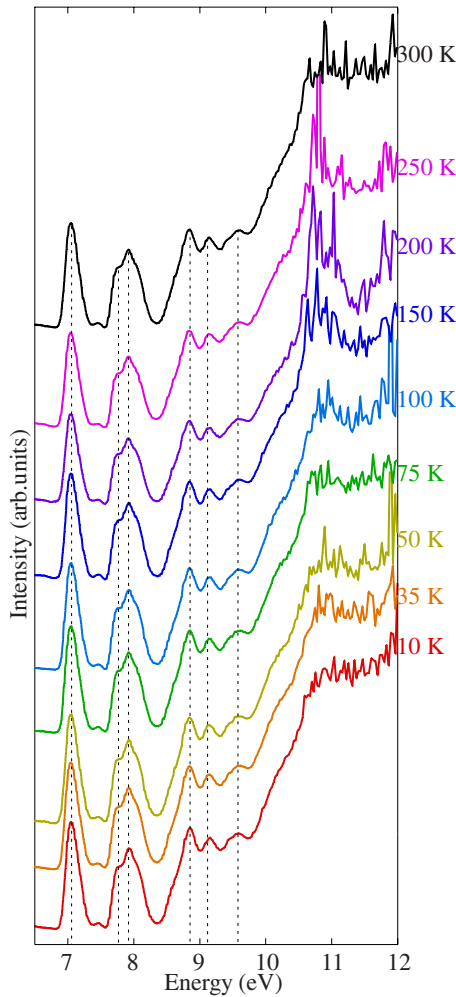


FIG. 6. (Color online) Temperature dependence of the  $4f^3$ - $4f^25d^1$  absorption spectra for  $\text{Nd}^{3+}$  in  $\text{LiYF}_4$ .

To clarify the peak origins for  $\text{U}^{3+}$  in  $\text{LiYF}_4$ , configuration analysis of the many-electron wave functions was performed. The multiplet energy levels of  $\text{U}^{3+}$  in  $\text{LiYF}_4$  in the range 2.0–6.0 eV are shown in Fig. 8, along with the oscillator strengths and the theoretical spectrum for the transitions from the lowest level. In Fig. 4, the peaks in both the experimental and theoretical absorption spectra are denoted as A–J.

Peaks A–C mainly originate from transitions to the  $(5f_{5/2})^2(6d_{1b})^1$  configuration and peak D mainly originates from transitions to the  $(5f_{5/2})^1(5f_{7/2})^1(6d_{1b})^1$  configuration. Thus, the splitting between A–C and D can be attributed to spin-orbit interactions of U  $5f$  orbitals and transitions to two-electron excitation states based on a shake-up process. Peaks E–G can be mainly attributed to transitions to  $(5f_{5/2})^1(5f_{7/2})^1(6d_{1b})^1$ ,  $(5f_{7/2})^2(6d_{1b})^1$ , and  $(5f_{5/2})^2(6d_a)^1$  configurations. In addition, the  $(5f_{5/2})^1(5f_{7/2})^1(6d_a)^1$  configuration is also slightly mixed. Thus, the splitting between peaks A–C and peaks E–G can be attributed to both the crystal field of the U  $6d$  orbitals and spin-orbit splitting of U  $5f$  orbitals. Peaks H and I mainly originate from transitions to the  $(4f_{5/2})^1(4f_{7/2})^1(5d_a)^1$  configuration. In addition, the  $(5f_{5/2})^1(5f_{7/2})^1(6d_{1b})^1$ ,  $(5f_{7/2})^2(6d_{1b})^1$ , and  $(5f_{5/2})^2(6d_a)^1$  configurations are slightly mixed. Thus, the splitting between

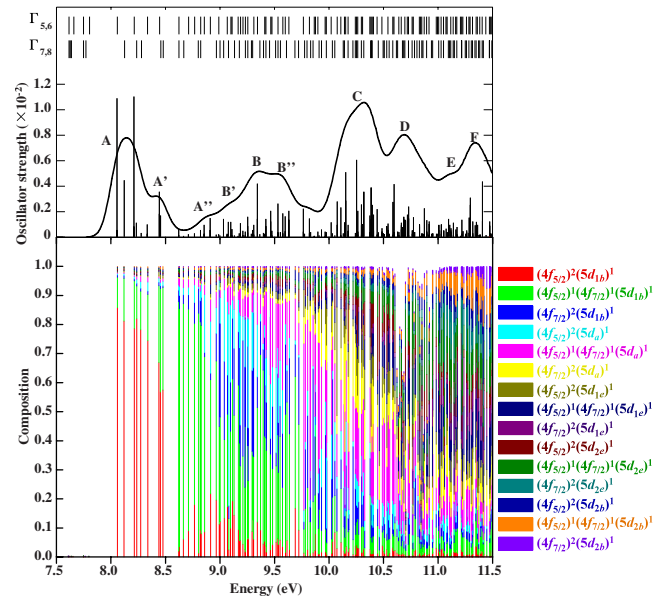


FIG. 7. (Color online) Configuration analysis of the many-electron wave functions for the  $4f^3$ - $4f^25d^1$  transitions of  $\text{Nd}^{3+}$  in  $\text{LiYF}_4$ .

the bands of peaks E–G and the bands of peaks H and I is mainly attributed to spin-orbit interactions of the U  $5f$  orbitals. For peak J, which has the same origin as peaks H and I, additional crystal-field components are mixed, and a large configuration interaction occurs.

### C. Estimation of lattice relaxation for $\text{Pr}^{3+}$ in $\text{LiYF}_4$

First, we discuss the optimized structures of the  $\text{LiYF}_4$  host crystal and  $\text{Pr}^{3+}$ -doped  $\text{LiYF}_4$ . A search for the global minimum on the energy surface was conducted using a first-

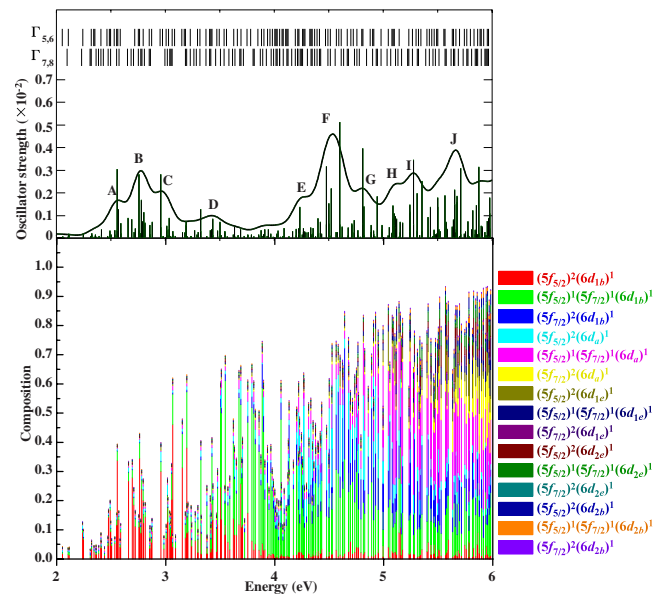


FIG. 8. (Color online) Configuration analysis of the many-electron wave functions for the  $5f^3$ - $5f^26d^1$  transitions of  $\text{U}^{3+}$  in  $\text{LiYF}_4$ .

TABLE III. Experimental and theoretical crystal parameters of LiYF<sub>4</sub> crystal.

	Experiment <sup>a</sup>	Calculation
Lattice constants $a, b$ (Å)	5.164	5.192 (100.5%)
Lattice constant $c$ (Å)	10.741	10.785 (100.2%)
Cell volume (Å <sup>3</sup> )	286.429	290.733 (101.5%)
Bond length 1 (Å)	2.244	2.252 (100.4%)
Bond length 2 (Å)	2.297	2.317 (100.9%)
Anion parameter $x$	0.2183	0.2187 (100.2%)
Anion parameter $y$	0.5855	0.5855 (100.0%)
Anion parameter $z$	0.5427	0.5448 (100.4%)

<sup>a</sup>Reference 76.

principles total-energy and molecular-dynamics method with the CASTEP code. To confirm the accuracy of the approach, the lattice parameters and all atomic positions of the unit cell of pure LiYF<sub>4</sub> were optimized, and compared to the experimental values.<sup>76</sup> Theoretical and experimental crystal parameters are listed in Table III. In addition, the ratio (100 × calculation/experiment) of these values is listed in parenthesis. For the LiYF<sub>4</sub> crystal, the anion parameters  $x$ ,  $y$ , and  $z$  have a very important role in determining the crystal structure, since the F<sup>−</sup> anions occupy a low-symmetry site, while the cations (Li<sup>+</sup>, Y<sup>3+</sup>) occupy a high-symmetry site. Since the

difference between the experimental and theoretical values of the crystal parameters listed in Table III, except for the cell volume, was within 1%, the optimized structure of the LiYF<sub>4</sub> host crystal was in good agreement with the experimentally determined structure. Regarding the cell volume, since the ratio was dependent upon the cube of the lattice constant, 1.5% overestimation of the cell volume was reasonable.

Next, we optimized the local structure around the Pr<sup>3+</sup> ions in Pr<sup>3+</sup>-doped LiYF<sub>4</sub>. In this calculation, one Y<sup>3+</sup> ion in the 2 × 2 × 1 supercell was substituted by a Pr<sup>3+</sup> ion. This supercell contained 96 atoms, and contained 6.25% of the Y<sup>3+</sup> ions in LiYF<sub>4</sub>. All atomic positions were relaxed, while keeping the lattice parameters fixed at their theoretical values, obtained above for pure LiYF<sub>4</sub>. The estimated distances between the central Y<sup>3+</sup> or Pr<sup>3+</sup> and the nearest-neighboring eight F<sup>−</sup> and neighboring cations (Y<sup>3+</sup> and Li<sup>+</sup>) are listed in Table IV, along with the experimental values. The estimated bond lengths between Y<sup>3+</sup> or Pr<sup>3+</sup> and the first nearest neighboring F<sup>−</sup> are also plotted in Fig. 9. For comparison, the Pr<sup>3+</sup>-F<sup>−</sup> bond lengths estimated by isotropic relaxation using the Shannon's ionic radii are also listed. The details of this estimation by isotropic relaxation were described in Refs. 63 and 66.

There are two types of Y<sup>3+</sup>-F<sup>−</sup> bonds in pure LiYF<sub>4</sub> host crystal, because of the S<sub>4</sub> symmetry of the Y<sup>3+</sup> site, with bond lengths of 2.244 Å for four of the bonds and 2.297 Å

TABLE IV. Distances between the central Y<sup>3+</sup> or Pr<sup>3+</sup> and the nearest-neighboring eight F<sup>−</sup> or the neighbor cations, Y<sup>3+</sup> and Li<sup>+</sup>.

	LiYF <sub>4</sub> host			Pr <sup>3+</sup> :LiYF <sub>4</sub>	
	Expt. (Ref. 56) (Å)	DFT Calc. <sup>a</sup> (Å)		Isotropic (Å)	DFT Calc. (Å)
Y-F1	2.244	2.252	Pr-F1	2.347	2.315
					2.315
					2.315
					2.315
Y-F2	2.297	2.317	Pr-F2	2.403	2.337
					2.338
					2.338
					2.338
Y-Li1	3.652	3.671	Pr-Li1		3.667
Y-Li2	3.652	3.671	Pr-Li2		3.667
Y-Li3	3.652	3.671	Pr-Li3		3.667
Y-Li4	3.652	3.671	Pr-Li4		3.667
Y-Li5	3.725	3.743	Pr-Li5		3.741
Y-Li6	3.725	3.743	Pr-Li6		3.741
Y-Li7	3.725	3.743	Pr-Li7		3.739
Y-Li8	3.725	3.743	Pr-Li8		3.741
Y-Y1	3.725	3.743	Pr-Y1		3.739
Y-Y2	3.725	3.743	Pr-Y2		3.739
Y-Y3	3.725	3.743	Pr-Y3		3.739
Y-Y4	3.725	3.743	Pr-Y4		3.739

<sup>a</sup>Reference 76.

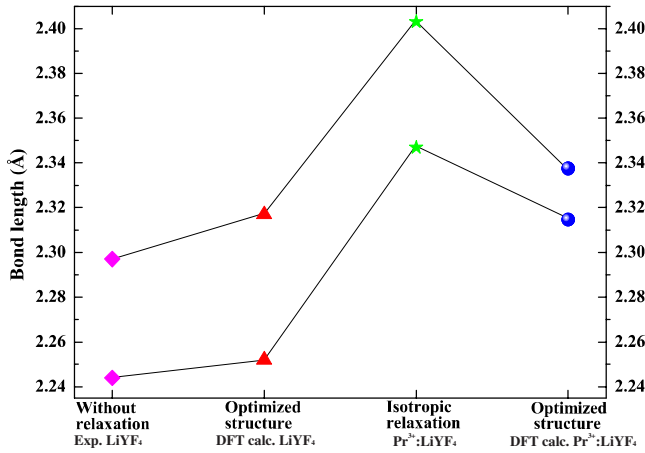


FIG. 9. (Color online) Bond lengths between  $Y^{3+}$  or  $Pr^{3+}$  and the first nearest-neighbor  $F^-$ .

for the other four. The optimized  $Y^{3+}$ - $F^-$  bond lengths in  $LiYF_4$  after structural optimization by first-principles calculation were 2.252 Å for four of the bonds and 2.317 Å for the other four. The difference between the theoretical and experimental values was within 1%. The  $Pr^{3+}$ - $F^-$  bond lengths estimated by isotropic relaxation for  $Pr^{3+}$ -doped  $LiYF_4$  were 2.347 Å for four of the bonds and 2.403 Å for the other four, indicating that all bonds were extended by 4.6% from their original lengths. On the other hand, structural optimization by DFT calculation of a  $Pr^{3+}$ -doped supercell indicated that the local structure around the  $Pr^{3+}$  site was slightly distorted, and the point symmetry of the  $Pr^{3+}$  sites was reduced from the original  $S_4$  to  $C_1$ . However, these changes were very small and the point symmetry of the local site nearly equaled the original  $S_4$  symmetry. The displacement magnitudes of the  $Pr^{3+}$ , eight  $F^-$ , eight  $Li^+$ , and four  $Y^{3+}$  are plotted in Fig. 10, as are the projections of the points onto each plane. The red, blue, yellow, and green spheres represent praseodymium, yttrium, lithium, and fluorine, re-

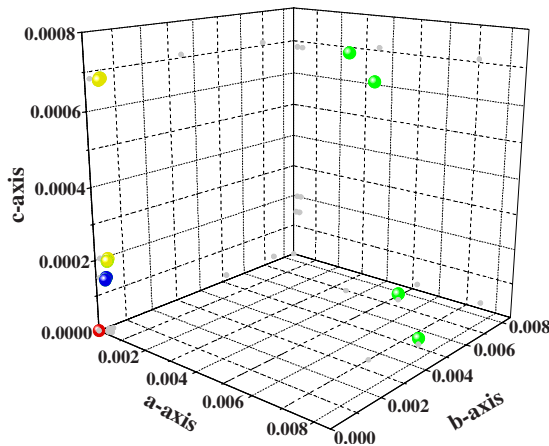


FIG. 10. (Color online) Displacement magnitudes of  $Pr^{3+}$  and eight  $F^-$ . The absolute values for the differences of internal coordinates are plotted, and their projections onto the planes are plotted. The red, blue, yellow, and green spheres represent praseodymium, yttrium, lithium, and fluorine, respectively. The gray points represent projections.

spectively. The gray points are the projection points. The displacement magnitudes of the first nearest eight  $F^-$  were within 0.008 Å for the  $a$  and  $b$  axes, and within 0.0008 Å for the  $c$  axis. For the first-nearest-neighboring cations,  $Y^{3+}$  and  $Li^+$ , the displacement magnitudes were much smaller than that of  $F^-$ , and the values were within 0.0007 Å for all axes. Therefore, the lattice relaxation and structural distortion around the  $Pr^{3+}$  site due to the substitution were very small for  $Pr^{3+}$  impurities in the  $LiYF_4$  host crystal.

#### D. Multiplet energy levels and absorption spectra $Pr^{3+}$ in $LiYF_4$

First, we investigated the effects of the exchange-correlation interaction, the Breit term, and lattice relaxation on the multiplet energies. In the present work, as identified above, six different Hamiltonians were examined. The  $^1S_0$  energy level, which is the highest energy level of the  $4f^2$  configuration ( $^1S_0$ ), the lowest energy level of the  $4f^15d^1$  configuration ( $E_{4f5d1st}$ ), the barycenter of multiplet energy levels for the  $4f^15d^1$  configuration ( $E_{5d \text{ barycenter}}$ ), and the splitting of multiplet energy levels for the  $4f^15d^1$  configuration ( $\Delta E_{5d}$ ) are listed in Table V. These evaluations were carried out using three different models: a model without lattice relaxation (nonrelaxation model), an isotropic relaxation model with adjusted bond lengths according to the Shannon's ionic radii (isotropic relaxation model), and an optimized structure model based on DFT calculations (optimized structure model). These data are also plotted in Fig. 11.

The  $^1S_0$  state was almost insusceptible to lattice relaxation in all Hamiltonians. This was natural because the  $4f^2$  configurations are relatively uninfluenced by the crystal field. Comparing the different Hamiltonians, the effect of the Breit term on the  $^1S_0$  state was about 0.02 eV, while the effect of the exchange-correlation potential on the  $^1S_0$  state can be ignored. In the  $4f^15d^1$  configuration, on the other hand, the lattice relaxation effects can be perceived with the  $E_{4f5d1st}$ ,  $E_{5d \text{ barycenter}}$ , and  $\Delta E_{5d}$  Hamiltonians, and these effects were about 0.15–0.30 eV. Since the  $Pr^{3+}$   $5d$  orbitals are strongly affected by the crystal fields, the changes in bond lengths had obvious effects. Consequently, the effects of the crystal field on the  $4f^15d^1$  configuration were about ten times the effect on the  $4f^2$  configuration. In addition, for the  $4f^15d^1$  configuration, the effects of the exchange-correlation potentials were not negligible. Since  $E_{4f5d1st}$  and  $E_{5d \text{ barycenter}}$  depended significantly on the exchange-correlation potentials, while  $\Delta E_{5d}$  varied little between the different exchange-correlation potentials, the multiplet energy levels for the  $4f^15d^1$  configuration calculated using the VWN or RVWN potentials shifted to a lower energy than those calculated using the  $X\alpha$  potential. The effects of the Breit term on the multiplet energy levels were vanishingly small. However, these theoretical values were overestimated compared to the experimental values. The experimental  $^1S_0$  energy level and  $E_{4f5d1st}$  were determined by VUV absorption spectroscopy, and were 5.94 eV (209 nm) and 5.79 eV (214 nm), respectively. Comparisons between the experimental values and theoretical values will be discussed later.

Next, we discuss the theoretical and experimental  $4f^2$ - $4f^15d^1$  absorption spectra for  $Pr^{3+}$  in  $LiYF_4$ . Figure 12

TABLE V. The  $^1S_0$  energy level ( $^1S_0$ ), the lowest energy level of the  $4f^{n-1}5d^1$  configuration ( $E_{4f5d1st}$ ), the barycenter of multiplet energy levels for the  $4f^{n-1}5d^1$  configuration ( $E_{5d \text{ barycenter}}$ ), and the splitting of multiplet energy levels for the  $4f^{n-1}5d^1$  configuration ( $\Delta E_{5d}$ ) calculated by three different models and six different Hamiltonians.

Nonrelaxation model	$^1S_0$ (eV)	$E_{4f5d1st}$ (eV)	$E_{5d \text{ barycenter}}$ (eV)	$\Delta E_{5d}$ (eV)
$H_{DC-X\alpha}$	7.65	8.16	10.55	5.25
$H_{DCB-X\alpha}$	7.64	8.16	10.55	5.25
$H_{DC-VWN}$	7.64	7.49	9.88	5.26
$H_{DCB-VWN}$	7.63	7.49	9.87	5.26
$H_{DC-RVWN}$	7.64	7.46	9.84	5.27
$H_{DCB-RVWN}$	7.63	7.45	9.84	5.27
Isotropic relaxation model	$^1S_0$ (eV)	$E_{4f5d1st}$ (eV)	$E_{5d \text{ barycenter}}$ (eV)	$\Delta E_{5d}$ (eV)
$H_{DC-X\alpha}$	7.65	8.31	10.36	4.71
$H_{DCB-X\alpha}$	7.63	8.31	10.36	4.70
$H_{DC-VWN}$	7.64	7.65	9.69	4.70
$H_{DCB-VWN}$	7.62	7.64	9.69	4.70
$H_{DC-RVWN}$	7.64	7.62	9.66	4.70
$H_{DCB-RVWN}$	7.62	7.61	9.66	4.70
Optimized structure model	$^1S_0$ (eV)	$E_{4f5d1st}$ (eV)	$E_{5d \text{ barycenter}}$ (eV)	$\Delta E_{5d}$ (eV)
$H_{DC-X\alpha}$	7.65	8.25	10.43	4.96
$H_{DCB-X\alpha}$	7.63	8.25	10.43	4.96
$H_{DC-VWN}$	7.64	7.58	9.76	4.96
$H_{DCB-VWN}$	7.62	7.58	9.76	4.96
$H_{DC-RVWN}$	7.64	7.55	9.73	4.97
$H_{DCB-RVWN}$	7.62	7.55	9.72	4.97

shows the Hamiltonian dependence of the theoretical  $4f^2-4f^15d^1$  absorption spectra (a) and the effect of lattice relaxation on the theoretical  $4f^2-4f^15d^1$  absorption spectra (b). The Hamiltonian dependence was investigated using the optimized structure model and the evaluation of lattice relaxation was performed using  $H_{DCB-RVWN}$ .

Since the peak position energies reflected the multiplet energy, the effects of different Hamiltonians on the spectra had the same tendency as the multiplet energy levels. In addition, the overall features of the spectral shape were completely Hamiltonian independent. The effects of lattice relaxation on the spectra also had the same tendency as the multiplet energy levels. However, the overall features of the spectral shape differed. The lower energy peaks (A-C) were nearly the same while the higher energy peaks (C' and D) were different. The differences were due to the relatively small difference in the crystal-field effects of isotropic relaxation in the optimized structure models relative to the non-relaxed model.

The experimental absorption spectrum at 10 K and the theoretical absorption spectra calculated using three models with the  $H_{DCB-RVWN}$  Hamiltonian are shown in Fig. 13. The

numerical data representing these spectra are also listed in Table VI. As previously mentioned, since the absolute multiplet energy levels were overestimated, the absolute transition energy was shifted by the orbital energy difference between the single-electron orbitals of the Slater transition state<sup>91</sup> as a reference.<sup>68</sup>

In the experimental absorption spectrum, five major peaks (A–D and H) were observed. Among these, peaks A–D were due to the  $4f^2-4f^15d^1$  transition of  $\text{Pr}^{3+}$ . Peak H was due to  $\text{LiYF}_4$  host absorption. Absorption peak D seemed to overlap with the host absorption. Thus, the intensity of peak D was deceptively high. Peak B was split into two peaks with a 0.16 eV splitting width. The peak energy separation between peaks A and B was about 0.96 eV, the separation between peaks B and C was about 0.95 eV, and the separation between peaks A and C was about 1.91 eV. On the other hand, subpeaks A', B', and C' were only observed at low temperatures. The peak energy separation between peaks A and A' was about 0.20 eV, the separation between peaks B and B' was about 0.46 eV, and the separation between peaks C and C' was about 0.33 eV. Using the nonrelaxation model, the splitting magnitude between peaks was overestimated compared to the experimental spectrum. This overestimation was due to the overestimation of the crystal fields, because the splitting between A and B, A and C, and B and C reflected the crystal field, which will be explained later. For the isotropic relaxation model, on the other hand, the splitting magnitude between the peaks was underestimated compared to the experimental splitting. This indicates that the crystal fields were underestimated in this model. Of these two models, the optimized structure model reproduced the experimental splitting magnitude quite well. Therefore, the evaluation of the crystal field was reasonably correct when using the optimized model.

Figure 14 shows the experimental  $4f^2-4f^15d^1$  absorption spectra for  $\text{Pr}^{3+}$  in  $\text{LiYF}_4$  measured at 10, 35, 50, 75, 100, 150, 200, 250, and 300 K. The inset represents a magnified view around the A and A' peaks (5.5 eV–6.5 eV) measured at 10 K. Five major peaks (A–D and H) were observed in all spectra. In addition, the  $^1S_0$  state, which is the highest state of the  $4f^2$  configuration, was observed at 5.94 eV (209 nm) at low temperature. This value is consistent with other studies. The  $^1S_0$  level was reported to be around 5.95 eV (Ref. 92) from experiment, and 5.85 (Ref. 93) or 6.05 eV (Ref. 94) from semiempirical calculations. The temperature dependences of the absorption spectra were also observed experimentally. As shown in Fig. 14, peak B in the experimental spectra strongly depended upon temperature. In addition, subpeaks A', B', and C' were only observed at low temperatures.

To clarify the origins of these peaks, we performed a configuration analysis of the many-electron wave functions. The results are shown in Fig. 15. The oscillator strengths of the absorption spectrum for transitions from the lowest state and the configuration compositions for each level are shown in the figure. The Pr 5d level split into 1b, a, e, and 2b from the lower level according to the irreducible representations of  $S_4$  symmetry. Also, the e state split slightly, due to spin-orbit interactions. In the present calculation, since lattice relaxation was considered, the local symmetry of the  $\text{Pr}^{3+}$  site was



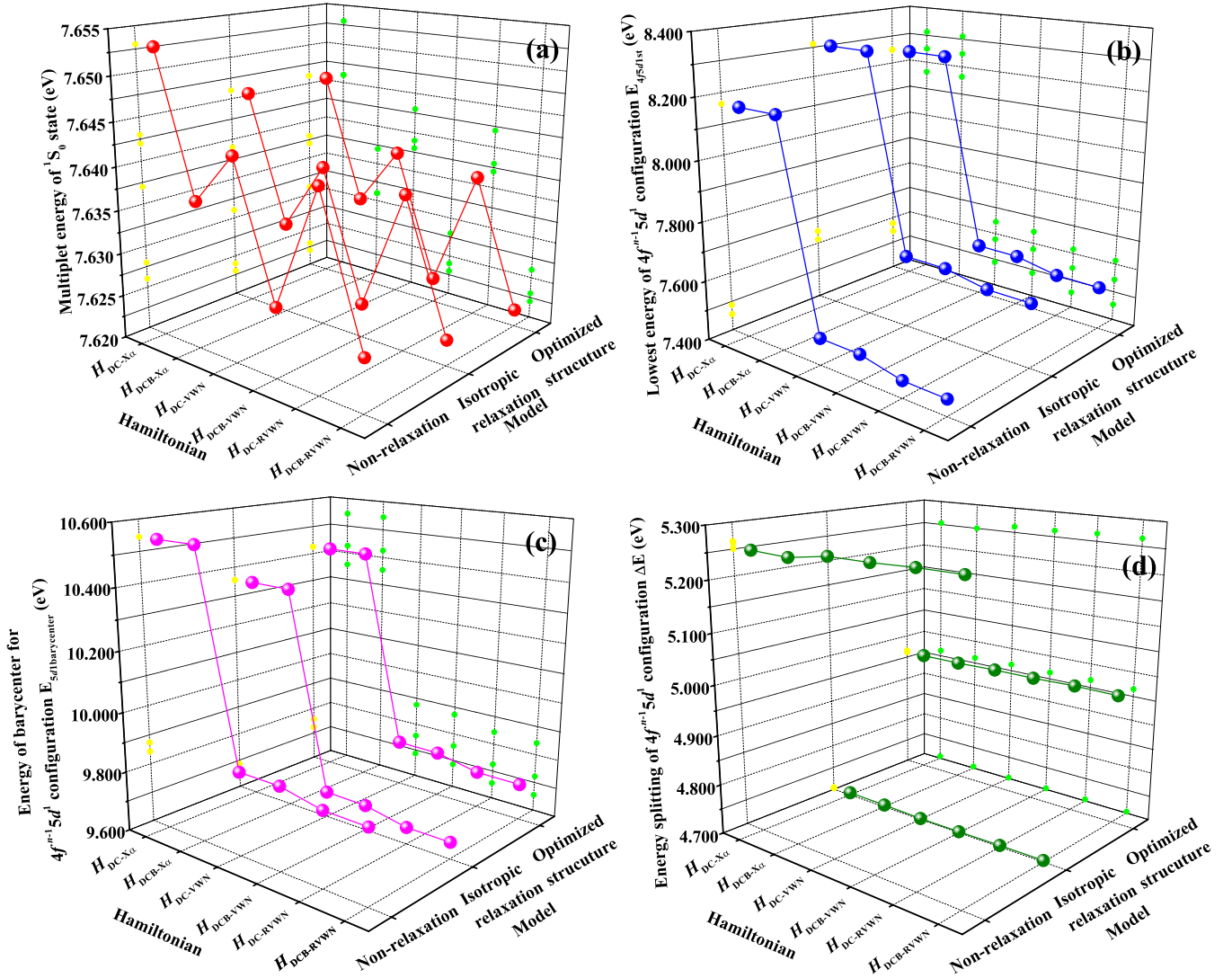


FIG. 11. (Color online) (a) The  $^1S_0$  energy level ( $^1S_0$ ), (b) the lowest energy level of the  $4f^{m-1}5d^1$  configuration ( $E_{4f5d1st}$ ), (c) the barycenter of multiplet energy levels for the  $4f^{m-1}5d^1$  configuration ( $E_{5d \text{ barycenter}}$ ), and (d) the splitting of multiplet energy levels for the  $4f^{m-1}5d^1$  configuration ( $\Delta E_{5d}$ ) calculated using three different models and six different Hamiltonians. The light green and yellow points represent projection points on different planes.

$C_1$ . However, since these distortions were very small, the irreducible representation of  $S_4$  symmetry was used in a straightforward manner. In addition, the theoretical absorption spectrum and the configuration compositions for each level were calculated using the optimized structure model with the  $H_{DCB-RVWN}$  Hamiltonian.

Peak A corresponds to transitions to the levels at 5.26 and 5.28 eV, and the configuration analysis indicated that the composition of the  $(4f_{5/2})^1(5d_{1b})^1$  configuration was greater than 90%. On the other hand, peak A' corresponds to transitions to the three levels at 5.60, 5.69, and 5.74 eV. The main component in this peak was  $(4f_{7/2})^1(5d_{1b})^1$ , with a

TABLE VI. Numerical data from the experimental absorption spectrum at 10 K and the theoretical absorption spectra calculated using three models with  $H_{DCB-RVWN}$ .

	A (eV)	A' (eV)	B (eV)	B' (eV)	C (eV)	C' (eV)	D (eV)
Nonrelaxation	5.17	5.53	6.30	6.90	7.36	7.70	8.14
Isotropic	5.29	5.66	6.21	6.76	7.13	7.41	7.80
Optimized	5.29	5.66	6.29	6.86	7.23	7.55	7.98
Experiment	5.79	5.99	6.76	7.22	7.70	8.04	~8.32
			6.91				

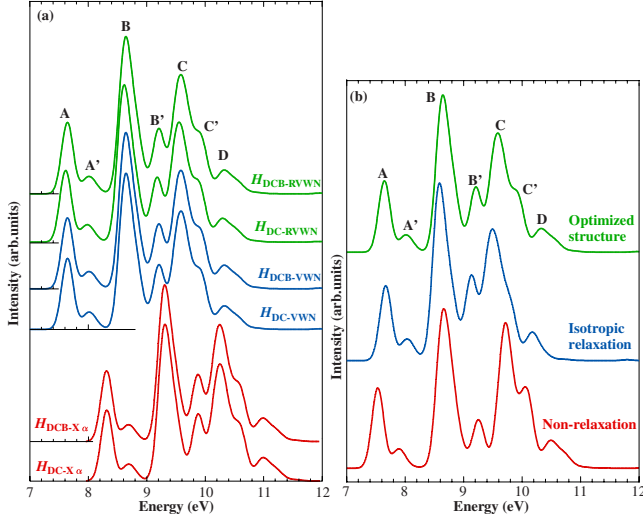


FIG. 12. (Color online) (a) Hamiltonian dependence of theoretical  $4f^2-4f^15d^1$  absorption spectra and (b) effect of the lattice relaxation on theoretical  $4f^2-4f^15d^1$  absorption spectra. The Hamiltonian dependence was investigated using the optimized structure model, and the evaluation of the lattice relaxation was performed using  $H_{\text{DCB-RVWN}}$ .

slight contribution from  $(4f_{5/2})^1(5d_a)^1$ . This indicates that the splitting between peaks A and A' originated from spin-orbit splitting of the Pr 4f levels. Similarly, peak B corresponds to transitions to the  $(4f_{5/2})^1(5d_a)^1$  configuration while peak B' corresponds to transitions to the  $(4f_{7/2})^1(5d_a)^1$  configuration. These results indicate that the splitting between peaks B and B' originated from spin-orbit splitting of Pr 4f levels. Compared to peaks A and B, the compositions of peaks C and D were complicated. Peak C corresponds to transitions to the mixed states of the  $(4f_{5/2})^1(5d_e)^1$  and  $(4f_{7/2})^1(5d_e)^1$  configurations, which corresponds to transitions from 4f states to Pr  $5d_e$  states in the one-electron picture. Since the main contributions to peak D were the  $(4f_{7/2})^1(5d_{1e})^1$ ,  $(4f_{5/2})^1(5d_{2e})^1$ ,  $(4f_{7/2})^1(5d_{2e})^1$ ,  $(4f_{5/2})^1(5d_{2b})^1$ , and  $(4f_{7/2})^1(5d_{2b})^1$  configurations, peak D can be represented as transitions from Pr 4f states to Pr  $5d_e$  and  $5d_{2b}$  states. For the entire spectra, configuration analysis clearly indicated that the separations among peaks A, B, and C were due to crystal-field splitting of the Pr 5d levels. The subpeaks can be attributed to transitions to two-electron excitation states, which are based on the shake-up process.

The calculated oscillator strengths were on the order of  $10^{-3}-10^{-2}$ . Thus, the calculated absorption cross sections of  $\text{Pr}^{3+}$  in  $\text{LiYF}_4$  were on the order of  $10^{-20}-10^{-19} \text{ cm}^2$ . These values are in reasonable agreement with experimental values for  $\text{Pr}^{3+}$  in  $\text{LiLuF}_4$  (on the order of  $10^{-19} \text{ cm}^2$ ).<sup>95</sup> Although the host crystal was  $\text{LiLuF}_4$ , the results are comparable to the theoretical spectrum for  $\text{LiYF}_4$ , since the crystal structure of  $\text{LiLuF}_4$  is the same as that of  $\text{LiYF}_4$ , but with slightly different lattice parameters.<sup>96</sup> However, since the ionic radii of  $\text{Y}^{3+}$  and  $\text{Lu}^{3+}$  are slightly different, the lattice relaxation effects are different in the two host crystals. Consequently, the absorption cross sections may vary slightly between the two host crystals.

Finally, we discuss the temperature dependence of the experimental spectra. Figure 16 shows the calculated absorp-

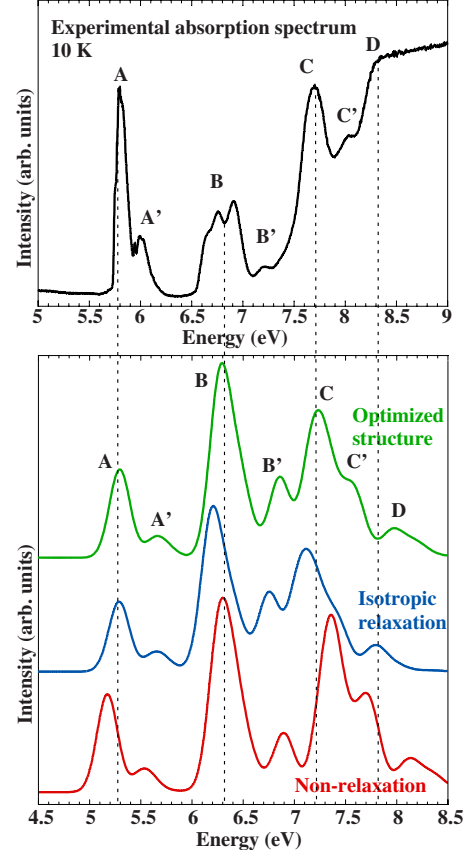


FIG. 13. (Color online) Experimental absorption spectrum at 10 K and theoretical absorption spectra calculated using three different models with  $H_{\text{DCB-RVWN}}$ .

tion spectra from two different initial states (bottom panel) and experimental spectra at 10, 100, and 300 K (upper panel). The absorption spectrum from the lowest level of the ground state  $^3\text{H}_4$  (at 0 eV) and from the second-lowest  $^3\text{H}_4$  level (at 0.0261 eV) were calculated using the optimized model with the  $H_{\text{DCB-RVWN}}$  Hamiltonian.

Peak B and subpeaks A' and B' were temperature dependent in the experimental spectra. Peak B<sub>2</sub> was dominant in the experimental absorption spectra at low temperature while peak B<sub>1</sub> became dominant with rising temperature. Peak B in the theoretical absorption spectrum from the second-lowest  $^3\text{H}_4$  level shifted to a slightly lower energy with respect to the peak from the lowest level of the ground state  $^3\text{H}_4$ . As a result, peak B of the experimental spectra split into two peaks (B<sub>1</sub> and B<sub>2</sub>). Since the intensities of subpeaks A' and B' of the theoretical absorption spectra weakened with increasing temperature, the temperature dependence of subpeaks A' and B' of the experimental spectra can be attributed to thermal excitation. In addition, since phonon coupling effects would also become progressively stronger in the experimental spectra with increasing temperature, the spectra would broaden. Therefore, the temperature dependence of the experimental spectra was due to both thermal excitation and phonon effects.

## V. CONCLUSION

We performed both experimental and theoretical investigation of the  $4f^n-4f^{n-1}5d^1$  transitions of  $\text{Pr}^{3+}$ ,  $\text{Nd}^{3+}$ , and  $\text{U}^{3+}$

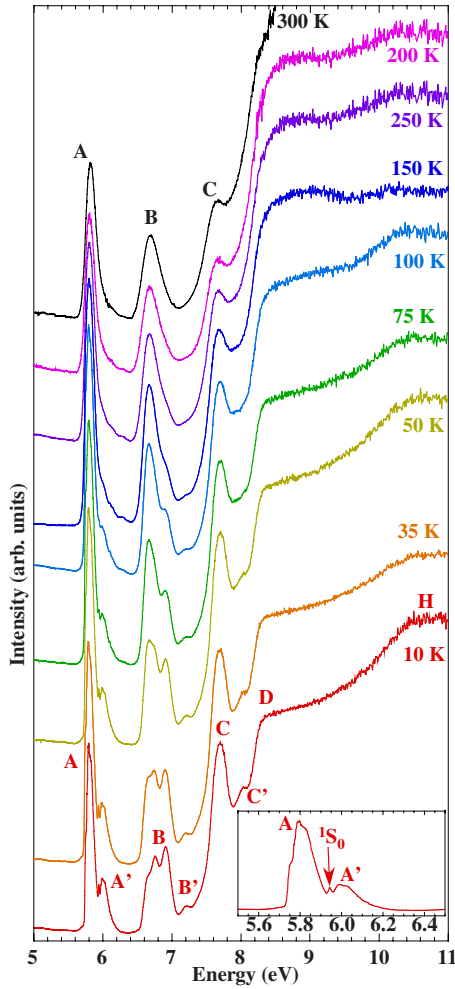


FIG. 14. (Color online) Experimental  $4f^2-4f^15d^1$  absorption spectra for  $\text{Pr}^{3+}$  in  $\text{LiYF}_4$  measured at 10, 35, 50, 75, 100, 150, 200, 250, and 300 K. The inset represents the magnified view around peaks A and A' (5.5–6.5 eV), measured at 10 K.

in  $\text{LiYF}_4$ . The multiplet energy levels and corresponding absorption spectra for  $\text{Nd}^{3+}$  and  $\text{U}^{3+}$  in  $\text{LiYF}_4$  were calculated using a first-principles many-electron method with  $H_{\text{DCB-RVWN}}$  Hamiltonian. For  $\text{Nd}^{3+}$  and  $\text{U}^{3+}$  in  $\text{LiYF}_4$ , the origins of the peaks in the absorption spectra were investigated by comparing the theoretical absorption spectra with experimental ones, and configuration analysis of the many-electron wave functions. Experimentally, we measured the  $4f^3-4f^25d^1$  absorption spectra for  $\text{Nd}^{3+}$  in  $\text{LiYF}_4$  using a SR light source at several temperatures.

The one-electron MO calculations indicated that the mixing between  $f$  and  $d$  states of  $\text{U}^{3+}:\text{LiYF}_4$  was larger than in  $\text{Nd}^{3+}:\text{LiYF}_4$  while the interactions with ligand  $\text{F } 2p$  orbitals were nearly the same.

Many-electron CI calculations indicated that the configuration interaction between the  $f^3$  configuration and the  $f^2d^1$  configuration in  $\text{U}^{3+}:\text{LiYF}_4$  was much stronger than in  $\text{Nd}^{3+}:\text{LiYF}_4$ . In addition, the  $5f^26d^1$  configuration of  $\text{U}^{3+}:\text{LiYF}_4$  lies at a considerably lower energy.

The theoretical absorption spectra of  $\text{Nd}^{3+}$  and  $\text{U}^{3+}$  in  $\text{LiYF}_4$  were in good agreement with experiment. The peak origins of both  $\text{Nd}^{3+}$  and  $\text{U}^{3+}$  were determined from configu-

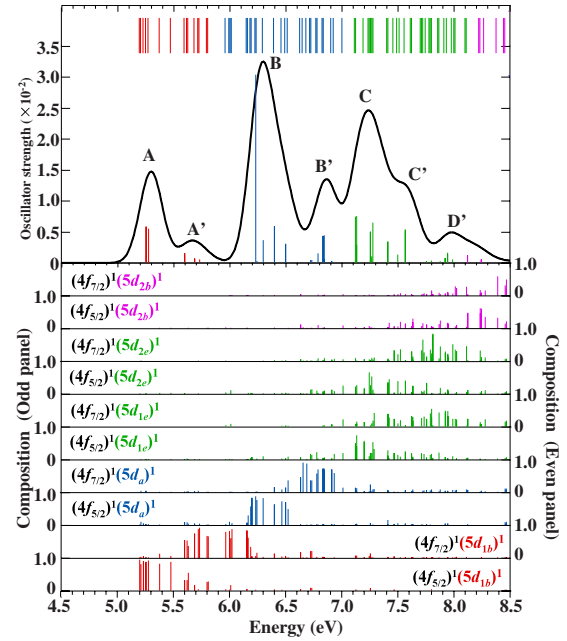


FIG. 15. (Color online) Configuration analysis of the many-electron wave functions for the  $4f^2-4f^15d^1$  transitions of  $\text{Pr}^{3+}$  in  $\text{LiYF}_4$ .

ration analysis of the many-electron wave functions. The splitting between peaks was affected by both spin-orbit interaction of  $f$  orbitals and the crystal fields of  $d$  orbitals. We found that the oscillator strengths of the  $4f^3-4f^25d^1$  transition

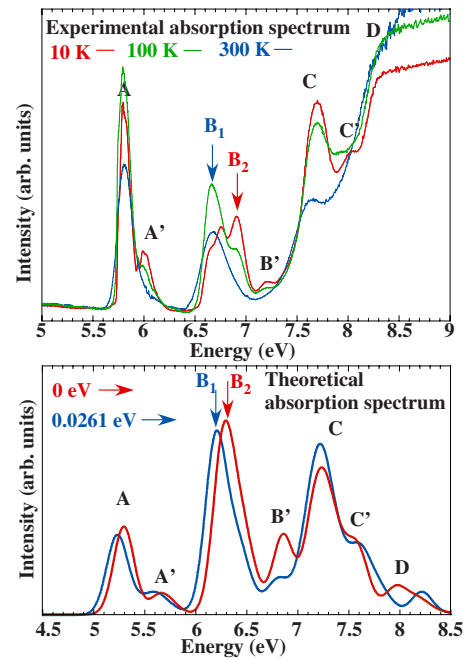


FIG. 16. (Color online) Theoretical absorption spectra from two different initial states (bottom panel), and experimental spectra at 10 (red), 100 (blue), and 300 K (green) (upper panel). The red and blue lines in the theoretical absorption spectra represent the calculated spectrum from the lowest level of the ground state  $^3\text{H}_4$  (at 0 eV), and from the second-lowest  $^3\text{H}_4$  level (at 0.0261 eV), respectively.

for  $\text{Nd}^{3+}$  in  $\text{LiYF}_4$  were slightly higher than those of the  $5f^3-5f^26d^1$  transition of  $\text{U}^{3+}$  in  $\text{LiYF}_4$ . The experimental absorption spectra for  $\text{Nd}^{3+}$  in  $\text{LiYF}_4$  measured at nine different temperatures indicated that the  $4f^3-4f^25d^1$  absorption spectra for  $\text{Nd}^{3+}$  in  $\text{LiYF}_4$  had no significant temperature dependence.

For  $\text{Pr}^{3+}$  in  $\text{LiYF}_4$ , we estimated the lattice relaxation effects due to the substitution of  $\text{Y}^{3+}$  by  $\text{Pr}^{3+}$  using a first-principles DFT calculation. Structural optimization calculations for a  $\text{Pr}^{3+}$ -doped supercell indicated that the local structure of the  $\text{Pr}^{3+}$  site was slightly distorted, and the point symmetry of the  $\text{Pr}^{3+}$  sites was reduced from the original  $S_4$  to  $C_1$ . However, these changes were very small and the point symmetry of the local site was nearly equal to the original  $S_4$  symmetry.

We also investigated the effects of the exchange-correlation interaction, the Breit term, and lattice relaxation on the multiplet energies using six different Hamiltonians. For the  $4f^2$  configurations, the lattice relaxation effects and the effects of the different Hamiltonians were very small, and could be ignored. For the  $4f^15d^1$  configuration, on the other hand, the lattice relaxation effects were perceptible when using  $E_{4f5d1st}$ ,  $E_{5d}$  barycenter, or  $\Delta E_{5d}$ , and were on the order of 0.15–0.30 eV. The overall shapes of the theoretical  $4f^2-4f^15d^1$  absorption spectra for  $\text{Pr}^{3+}$  in  $\text{LiYF}_4$  were independent of the Hamiltonian.

The  $4f^2-4f^15d^1$  absorption spectra for  $\text{Pr}^{3+}$  in  $\text{LiYF}_4$  were measured at 10, 35, 50, 75, 100, 150, 200, 250, and 300 K at

UVSOR BL1B, and were compared to theoretical absorption spectra. Although the absolute multiplet energy levels were overestimated, the overall features of the theoretical absorption spectra well reproduced the experimental spectra. In addition, by performing the Slater's transition state calculation, the absolute transition energies for the theoretical spectra were also in reasonable agreement with experimental values. The origins of the experimental spectra were clarified by performing configuration analysis of the many-electron wave functions. The configuration analysis clearly indicated that the separations among peaks A, B, and C were due to crystal-field splitting of the  $\text{Pr } 5d$  levels while splitting between the main peaks and subpeaks was due to spin-orbit interaction of the  $\text{Pr } 4f$  levels. The subpeaks were due to transitions to two-electron excitation states based on a shake-up process. Finally, theoretical calculations indicated that the temperature dependence of the experimental spectra was due to both thermal excitation and phonon effects.

## ACKNOWLEDGMENTS

The authors are grateful to T. Ishii for valuable discussion. The present work was supported in part by the "Open Research Center" Project for Private Universities matching fund subsidy from MEXT (Ministry of Education, Culture, Sports, Science and Technology). This work was partly performed under the Joint Studies Program of the Institute for Molecular Science.

\*watanabe@vbl.nagoya-u.ac.jp

- <sup>1</sup>A. A. Kaminskii, H. J. Eichler, B. Liu, and P. Meindl, *Phys. Status Solidi A* **138**, K45 (1993).
- <sup>2</sup>W. Koehner, *Solid-State Engineering* (Springer-Verlag, New York, 1999).
- <sup>3</sup>M. Malinowski, M. F. Joubert, and B. Jacquire, *Phys. Rev. B* **50**, 12367 (1994).
- <sup>4</sup>A. Richter, E. Heumann, E. Osiac, G. Huber, W. Seelert, and A. Dening, *Opt. Lett.* **29**, 2638 (2004).
- <sup>5</sup>K. Hashimoto and F. Kannari, *Jpn. J. Appl. Phys., Part 2* **46**, 589 (2007).
- <sup>6</sup>S. Khiari, M. Velazquez, R. Moncorgé, J. L. Doualan, P. Camy, A. Ferrier, and M. Diaf, *J. Alloys Compd.* **451**, 128 (2008).
- <sup>7</sup>J. C. Krupa and M. Queffelec, *J. Alloys Compd.* **250**, 287 (1997).
- <sup>8</sup>M. Laroche, A. Braud, S. Girard, J. L. Doualan, R. Moncorgé, M. Thuau, and L. D. Merkle, *J. Opt. Soc. Am. B* **16**, 2269 (1999).
- <sup>9</sup>M. F. Reid, L. van Pieterse, R. T. Wegh, and A. Meijerink, *Phys. Rev. B* **62**, 14744 (2000).
- <sup>10</sup>L. van Pieterse, R. T. Wegh, A. Meijerink, and M. F. Reid, *J. Chem. Phys.* **115**, 9382 (2001).
- <sup>11</sup>L. van Pieterse, M. F. Reid, R. T. Wegh, S. Soverna, and A. Meijerink, *Phys. Rev. B* **65**, 045113 (2002).
- <sup>12</sup>Th. Tröster and V. Lavín, *J. Lumin.* **101**, 243 (2003).
- <sup>13</sup>P. S. Peijzel, P. Vergeer, A. Meijerink, M. F. Reid, L. A. Boatner, and G. W. Burdick, *Phys. Rev. B* **71**, 045116 (2005).

- <sup>14</sup>D. Wang, S. Huang, F. You, S. Qi, Y. Fu, G. Zhang, J. Xu, and Y. Huang, *J. Lumin.* **122-123**, 450 (2007).
- <sup>15</sup>B. Z. Malkin, O. V. Solov'yev, A. Yu. Malishev, and S. K. Saikin, *J. Lumin.* **125**, 175 (2007).
- <sup>16</sup>K. H. Yang and A. DeLuca, *Phys. Rev. B* **17**, 4246 (1978).
- <sup>17</sup>Z. Kollia, E. Sarantopoulou, A. C. Cefalas, C. A. Nicolaides, A. K. Naumov, V. V. Semashko, R. Y. Abdulsabirov, S. L. Korebleva, and M. A. Dubinskii, *J. Opt. Soc. Am. B* **12**, 782 (1995).
- <sup>18</sup>J. Thøgersen, J. D. Gill, and H. K. Haugen, *Opt. Commun.* **132**, 83 (1996).
- <sup>19</sup>J. S. Cashmore, S. M. Hooker, and C. E. Webb, *Appl. Phys. B: Lasers Opt.* **64**, 293 (1997).
- <sup>20</sup>Z. Kollia, E. Sarantopoulou, A. C. Cefalas, A. K. Naumov, V. V. Semashko, R. Y. Abdulsabirov, and S. L. Korebleva, *Opt. Commun.* **149**, 386 (1998).
- <sup>21</sup>Y. Guyot, S. Guy, and M. F. Joubert, *J. Alloys Compd.* **323-324**, 722 (2001).
- <sup>22</sup>A. Collombet, Y. Guyot, M. F. Joubert, M. Laroche, J. Margerie, R. Moncorgé, and E. Descroix, *Phys. Rev. B* **68**, 035115 (2003).
- <sup>23</sup>A. F. H. Librantz, L. Gomes, L. V. G. Tarelho, and I. M. Ranieri, *J. Appl. Phys.* **95**, 1681 (2004).
- <sup>24</sup>A. F. H. Librantz, L. Gomes, S. L. Baldochi, I. M. Ranieri, and G. E. Brito, *J. Lumin.* **121**, 137 (2006).
- <sup>25</sup>P. P. Sorokin and M. J. Stevenson, *Phys. Rev. Lett.* **5**, 557 (1960).
- <sup>26</sup>G. D. Boyd, R. J. Collins, S. P. S. Porto, A. Yariv, and W. A. Hargreaves, *Phys. Rev. Lett.* **8**, 269 (1962).



- <sup>27</sup>S. Cotton, *Lanthanide and Actinide Chemistry* (Wiley, West Sussex, 2006).
- <sup>28</sup>S. Hubert, E. Simoni, M. Louis, F. Auzel, D. Meichenin, and J. Y. Gesland, *J. Phys. IV* **04**, C4-393 (1994).
- <sup>29</sup>S. Hubert, E. Simoni, M. Louis, W. P. Zhang, and J. Y. Gesland, *J. Lumin.* **60-61**, 245 (1994).
- <sup>30</sup>S. Hubert, M. Louis, E. Simoni, and M. F. Reid, *J. Phys. II* **5**, 755 (1995).
- <sup>31</sup>E. Simoni, M. Louis, J. Y. Gesland, and S. Hubert, *J. Lumin.* **65**, 153 (1995).
- <sup>32</sup>E. Simoni, M. Louis, S. Hubert, and S. Xia, *Opt. Mater.* **4**, 641 (1995).
- <sup>33</sup>M. Louis, S. Hubert, E. Simoni, and J. Y. Gesland, *Opt. Mater.* **6**, 121 (1996).
- <sup>34</sup>L. Ning, Y. Jiang, S. Xia, and P. A. Tanner, *J. Phys.: Condens. Matter* **15**, 7337 (2003).
- <sup>35</sup>L. van Pieterson, M. F. Reid, G. W. Burdick, and A. Meijerink, *Phys. Rev. B* **65**, 045114 (2002).
- <sup>36</sup>G. Liu, in *Spectroscopic Properties of Rare Earths in Optical Materials* edited by G. Liu and B. Jacquier (Springer-Verlag, Berlin, 2005), Chap. 1; M. F. Reid, in *Spectroscopic Properties of Rare Earths in Optical Materials* edited by G. Liu and B. Jacquier (Springer-Verlag, Berlin, 2005), Chap. 2.
- <sup>37</sup>G. W. Burdick and M. F. Reid, in *Handbook on the Physics and Chemistry of Rare Earths*, edited by K. A. Gschneidner, Jr., J. C. G. Bunzli, and V. K. Pecharsky (North-Holland, Amsterdam, 2007), Vol. 37, Chap. 232.
- <sup>38</sup>W. Duan, R. M. Wentzcovitch, and K. T. Thomson, *Phys. Rev. B* **57**, 10363 (1998).
- <sup>39</sup>V. V. Mazurenko, A. N. Varaksin, V. G. Mazurenko, V. S. Kortov, and V. I. Anisimov, *Physica B* **344**, 385 (2004).
- <sup>40</sup>J. M. García-Lastra, M. T. Barriuso, J. A. Aramburu, and M. Moreno, *Phys. Rev. B* **72**, 113104 (2005).
- <sup>41</sup>J. M. García-Lastra, J. A. Aramburu, M. T. Barriuso, and M. Moreno, *Phys. Rev. B* **74**, 115118 (2006).
- <sup>42</sup>M. Moreno, M. T. Barriuso, J. A. Aramburu, P. García-Fernández, and J. M. García-Lastra, *J. Phys.: Condens. Matter* **18**, R315 (2006).
- <sup>43</sup>E. Gaudry, D. Cabaret, C. Brouder, I. Letard, A. Rogalev, F. Wilhelm, N. Jaouen, and P. Saintavit, *Phys. Rev. B* **76**, 094110 (2007).
- <sup>44</sup>E. Gaudry, A. Kiratisin, P. Saintavit, C. Brouder, F. Mauri, A. Ramos, A. Rogalev, and J. Goulon, *Phys. Rev. B* **67**, 094108 (2003).
- <sup>45</sup>E. Gaudry, D. Gabarer, P. Saintavit, C. Brouder, F. Mauri, J. Goulon, and A. Rogalev, *J. Phys.: Condens. Matter* **17**, 5467 (2005).
- <sup>46</sup>A. Trueba, J. M. García-Lastra, M. T. Barriuso, J. A. Aramburu, and M. Moreno, *Phys. Rev. B* **78**, 075108 (2008).
- <sup>47</sup>A. A. Bagatur'yants, I. M. Iskandarova, A. A. Knizhnik, V. S. Mironov, B. V. Potapkin, A. M. Srivastava, and T. J. Sommerer, *Phys. Rev. B* **78**, 165125 (2008).
- <sup>48</sup>T. Mizoguchi, I. Tanaka, S. Yoshioka, M. Kunisu, T. Yamamoto, and W. Y. Ching, *Phys. Rev. B* **70**, 045103 (2004).
- <sup>49</sup>I. Tanaka, T. Mizoguchi, and T. Yamamoto, *J. Am. Ceram. Soc.* **88**, 1203 (2005).
- <sup>50</sup>W. Y. Ching and P. Rulis, *Phys. Rev. B* **77**, 035125 (2008).
- <sup>51</sup>Z. Barandiarán and L. Seijo, *J. Chem. Phys.* **119**, 3785 (2003).
- <sup>52</sup>B. Ordejón, L. Seijo, and Z. Barandiarán, *J. Chem. Phys.* **119**, 6143 (2003).
- <sup>53</sup>L. Seijo and Z. Barandiarán, in *Relativistic Electronic Structure Theory: Part 2. Applications*, edited by P. Schwerdtfeger (Elsevier, Amsterdam, 2004), pp. 417–475.
- <sup>54</sup>F. Ruipérez, Z. Barandiarán, and L. Seijo, *J. Chem. Phys.* **123**, 244703 (2005).
- <sup>55</sup>J. L. Pascual, J. Schamps, Z. Barandiarán, and L. Seijo, *Phys. Rev. B* **74**, 104105 (2006).
- <sup>56</sup>J. L. Pascual, Z. Barandiarán, and L. Seijo, *Phys. Rev. B* **76**, 104109 (2007).
- <sup>57</sup>J. Gracia, L. Seijo, Z. Barandiarán, D. Curulla, H. Niemansverdiertm, and W. van Gennip, *J. Lumin.* **128**, 1248 (2008).
- <sup>58</sup>T. Ishii, K. Fujimura, K. Sato, M. G. Brik, and K. Ogasawara, *J. Alloys Compd.* **374**, 18 (2004).
- <sup>59</sup>T. Ishii, M. G. Brik, and K. Ogasawara, *J. Alloys Compd.* **380**, 136 (2004).
- <sup>60</sup>T. Ishii, K. Ogasawara, H. Adachi, P. Burmester, and G. Huber, *Int. J. Quantum Chem.* **99**, 488 (2004).
- <sup>61</sup>K. Ogasawara, S. Watanabe, H. Toyoshima, T. Ishii, M. G. Brik, H. Ikeno, and I. Tanaka, *J. Solid State Chem.* **178**, 412 (2005).
- <sup>62</sup>T. Ishii, *J. Chem. Phys.* **122**, 024705 (2005).
- <sup>63</sup>S. Watanabe, T. Ishii, K. Fujimura, and K. Ogasawara, *J. Solid State Chem.* **179**, 2438 (2006).
- <sup>64</sup>H. Yoshida, T. Yamazaki, H. Toyoshima, S. Watanabe, K. Ogasawara, and H. Yamamoto, *J. Electrochem. Soc.* **154**, J196 (2007).
- <sup>65</sup>K. Ogasawara, S. Watanabe, H. Toyoshima, and M. G. Brik, in *Handbook on the Physics and Chemistry of Rare Earths*, edited by K. A. Gschneidner, Jr., J. C. G. Bunzli, and V. K. Pecharsky (North-Holland, Amsterdam, 2007), Vol. 37, Chap. 231.
- <sup>66</sup>S. Watanabe and K. Ogasawara, *J. Phys. Soc. Jpn.* **77**, 084702 (2008).
- <sup>67</sup>R. D. Shannon, *Acta Crystallogr., Sect. A: Cryst. Phys., Diffraction, Theor. Gen. Crystallogr.* **32**, 751 (1976).
- <sup>68</sup>K. Ogasawara, T. Iwata, Y. Koyama, T. Ishii, I. Tanaka, and H. Adachi, *Phys. Rev. B* **64**, 115413 (2001).
- <sup>69</sup>H. Ikeno, I. Tanaka, T. Miyamae, T. Mishima, H. Adachi, and K. Ogasawara, *Mater. Trans.* **45**, 1414 (2004).
- <sup>70</sup>H. Ikeno, I. Tanaka, Y. Koyama, T. Mizoguchi, and K. Ogasawara, *Phys. Rev. B* **72**, 075123 (2005).
- <sup>71</sup>M. G. Brik, K. Ogasawara, H. Ikeno, and I. Tanaka, *Eur. Phys. J. B* **51**, 345 (2006).
- <sup>72</sup>H. Ikeno, T. Mizoguchi, Y. Koyama, Y. Kumagai, and I. Tanaka, *Ultramicroscopy* **106**, 970 (2006).
- <sup>73</sup>M. C. Payne, M. P. Teter, D. C. Allan, T. A. Arias, and J. D. Joannopoulos, *Rev. Mod. Phys.* **64**, 1045 (1992).
- <sup>74</sup>M. D. Segall, P. J. D. Lindan, M. I. J. Probert, C. J. Pickard, P. J. Hasnip, S. J. Clark, and M. C. Payne, *J. Phys.: Condens. Matter* **14**, 2717 (2002).
- <sup>75</sup>S. J. Clark, M. D. Segall, C. J. Pickard, P. J. Hasnip, M. I. J. Probert, K. Refson, and M. C. Payne, *Z. Kristallogr.* **220**, 567 (2005).
- <sup>76</sup>E. Garcia and R. R. Ryan, *Acta Crystallogr., Sect. C: Cryst. Struct. Commun.* **49**, 2053 (1993).
- <sup>77</sup>D. Vanderbilt, *Phys. Rev. B* **41**, 7892 (1990).
- <sup>78</sup>J. P. Perdew, K. Burke, and M. Ernzerhof, *Phys. Rev. Lett.* **77**, 3865 (1996).
- <sup>79</sup>H. Monkhorst and J. Pack, *Phys. Rev. B* **13**, 5188 (1976).
- <sup>80</sup>H. M. Evjen, *Phys. Rev.* **39**, 675 (1932).
- <sup>81</sup>A. Rosén, D. E. Ellis, H. Adachi, and F. W. Averill, *J. Chem. Phys.* **65**, 3629 (1976).

- <sup>82</sup>S. H. Vosko, L. Wilk, and M. Nusair, *Can. J. Phys.* **58**, 1200 (1980).
- <sup>83</sup>A. H. MacDonald and S. H. Vosko, *J. Phys. C* **12**, 2977 (1979).
- <sup>84</sup>S. Watanabe and K. Kamimura, *Mater. Sci. Eng., B* **3**, 313 (1989).
- <sup>85</sup>B. G. Breit, *Phys. Rev.* **34**, 553 (1929).
- <sup>86</sup>B. G. Breit, *Phys. Rev.* **39**, 616 (1932).
- <sup>87</sup>S. Sugano, Y. Tanabe, and H. Kamimura, *Multiplets of Transition-Metal Ions in Crystals* (Academic, New York, 1970).
- <sup>88</sup>B. R. E. Thoma, C. F. Weaver, H. A. Friedman, H. Insley, L. A. Harris, and H. A. Yakel, Jr., *J. Phys. Chem.* **65**, 1096 (1961).
- <sup>89</sup>R. S. Mulliken, *J. Chem. Phys.* **23**, 1833 (1955).
- <sup>90</sup>A. A. S. da Gama, G. F. de Sá, P. Porcher, and P. Caro, *J. Chem. Phys.* **75**, 2583 (1981).
- <sup>91</sup>J. C. Slater, *Quantum Theory of Molecules and Solids* (McGraw-Hill, New York, 1974), Vol. 4.
- <sup>92</sup>R. T. Wegh, A. Meijerink, R.-J. Lamminmäki, and J. Hölsä, *J. Lumin.* **87-89**, 1002 (2000).
- <sup>93</sup>M. G. Brik (private communication).
- <sup>94</sup>L. Esterowitz, F. J. Bartoli, and R. E. Allen, *Phys. Rev. B* **19**, 6442 (1979).
- <sup>95</sup>M. Laroche, J. L. Doualan, S. Girard, J. Margerie, and R. Moncorgé, *J. Opt. Soc. Am. B* **17**, 1291 (2000).
- <sup>96</sup>C. Keller and H. Schmutz, *J. Inorg. Nucl. Chem.* **27**, 900 (1965).